The evolution of the Kaapvaal craton: A multi-isotopic perspective from lithospheric peridotites from Finsch diamond mine

Qiao Shu[a,b,c,*], Gerhard P. Brey[a,d], D. Graham Pearson[b], Jingao Liu[e,b], Sally A. Gibson[f], Harry Becker[g]

[a] State Key Laboratory of Ore Deposit Geochemistry, Institute of Geochemistry, Chinese Academy of Sciences, Guiyang 550081, China
[b] Dept. of Earth and Atmospheric Sciences, University of Alberta, Edmonton, Canada
[c] CAS Center for Excellence in Comparative Planetology, China
[d] Institut für Geowissenschaften, Mineralogie, J. W. Goethe-Universität Frankfurt, Frankfurt, Germany
[e] State Key Laboratory of Geological Processes and Mineral Resources, China University of Geosciences, Beijing 100083, China
[f] Department of Earth Sciences, University of Cambridge, Cambridge CB2 3EQ, United Kingdom
[g] Institut für Geologische Wissenschaften, Freie Universität Berlin, Berlin, Germany

ABSTRACT

Accurately dating the formation and modification of Earth's sub-cratonic mantle still faces many challenges, primarily due to the long and complex history of depletion and subsequent metasomatism of this reservoir. In an attempt to improve this, we carried out the first study on peridotites from the Kaapvaal craton (Finsch Mine) that integrates results from Re-Os, Lu-Hf, Sm-Nd and Sr-isotope systems together with analyses of major-, trace- and platinum-group elements. The Finsch peridotites are well-suited for such a study because certain compositional features reflect they were highly depleted residues of shallow melting (1.5 GPa) at ambient Archean mantle temperatures. Yet, many of them have overabundant orthopyroxene, garnet and clinopyroxene compared to expected modal amounts for residues from partial melting. Finsch peridotites exhibit a wide range of rhenium depletion ages (T_{RD}) from present day to 2.7 Ga, with a prominent mode at 2.5 Ga. This age overlaps well with a Lu-Hf isochron of 2.64 Ga (εHf (t) = +26) which records silico-carbonatitic metasomatism of the refractory residues. This late Archean metasomatism is manifested by positive correlations of Pt/Ir and Pd/Ir with $^{187}Os/^{188}Os$ ratios and good correlations of modal amounts of silicates, especially garnet, with Os isotope ratios. These correlations suggest that the Highly Siderophile Elements (HSE) and incompatible element reenrichment and modal metasomatism result from one single major metasomatic event at late Archean.

Our detailed study of Finsch peridotites highlights the importance of using multiple isotopic systems, to constrain the ages of events defining the evolution of lithospheric mantle. The Re-Os isotope system is very effective in documenting the presence of Archean lithosphere, but only the oldest T_{RD} ages may accurately date or closely approach the age of the last major partial melting event. For a meaningful interpretation of the Re-Os isotope systematics the data must be combined with HSE patterns, trace-element compositions and ideally other isotopic systems, e.g. Lu-Hf. This is highlighted by the widespread evidence in Finsch peridotites of Pt, Pd and Re enrichment through significant Base Metal Sulfide (BMS) addition (mainly in the range of 0.002–0.08 wt%) that systematically shifts the mode of T_{RD} model ages to younger ages.

1. Introduction

The long-term stability of Archean cratons is primarily due to their refractory mantle roots that gained buoyancy after high degrees of partial melting (e.g. Jordan, 1975). Studies of peridotite xenoliths from the sub-cratonic mantle, brought to the surface by kimberlites have revealed its longevity and also complex evolutionary history (e.g. Nixon and Boyd, 1973; Dawson, 1984; Harte et al., 1987; Boyd, 1989; Pearson et al., 1995, Brey and Shu 2018). The main processes include primary melt depletion, metamorphism and multi-stage chemical overprinting (metasomatism) deep in the lithospheric mantle (e.g. Dawson, 1984; Harte et al., 1987; Simon et al., 2007; Gibson et al., 2008; Pearson and Wittig, 2014). The distinct geochemical behavior of the ^{187}Re-^{187}Os, ^{176}Lu-^{176}Hf, ^{147}Sm-^{143}Nd and ^{87}Rb-^{87}Sr radioactive isotope systems

during various geological processes has the potential to constrain the timing of these processes.

The Re-Os isotope system has the best potential to date melt depletion of mantle peridotites because Os is compatible and Re moderately incompatible during mantle melting (e.g. Rudnick and Walker, 2009). The incompatible lithophile trace element-based isotope systems (Sm-Nd and Rb-Sr) are very sensitive to overprinting in cratonic peridotites because metasomatic agents are generally highly enriched in these incompatible trace elements compared to the depleted mantle. These latter two isotope ratios may, however, constrain the timing and source of metasomatism because ancient enrichment events may result in distinctive isotopic reservoirs in the cratonic mantle (e.g. Pearson, 1999; Carlson et al., 1999; Shu and Brey, 2015). In peridotites the Lu-Hf isotope system is less sensitive to secondary overprinting than the Sm-Nd and Rb-Sr systems, primarily because the metasomatic agents in the deeper mantle originate from the garnet (grt) stability field and therefore have lower amounts of Lu than the infiltrated peridotite. This can lead either to the preservation of the Hf isotope composition from the period of partial melting, that of the metasomatic agent or a mix of both (Schmidberger et al., 2002; Pearson and Nowell, 2004; Simon et al., 2007). The Lu–Hf system may therefore be suitable for dating melt depletion (Wittig et al., 2007; Liu et al., 2012) or it can be applied to date ancient metasomatism events that completely reset the isotopic system in the cratonic mantle (Wittig et al., 2010; Shu et al., 2013; Shu and Brey, 2015).

Collectively, the combined application of multiple radioactive isotope systems to garnet peridotite xenoliths from a single locality can provide a more complete picture in understanding both the isotopic data and evolution of sub-cratonic mantle. A prerequisite is that demonstrable major and trace element equilibrium exists between their coexisting silicate minerals. In this paper, a suite of garnet peridotite xenoliths from the Finsch diamond mine on the Kimberley block of the Kaapvaal craton (electronic supplement Fig. S1) was selected for the analysis of the Re-Os, Lu-Hf, Sm-Nd isotope systems, the Sr isotope ratios in clinopyroxene and the highly siderophile element (HSE) concentrations in bulk rocks, silicate mineral separates and also Base Metal Sulfides. The petrology and major and trace element geochemistry has been well-characterized by Gibson et al. (2008) and Lazarov et al. (2009b and 2012a). For a subset of the samples, Lu-Hf and Sm-Nd isotope ratios were already measured by Lazarov et al. (2012b). The aim is to combine published geochemical and isotope data with our new isotope and HSE abundance data to constrain the timing of partial melting and metasomatism more tightly, and to further unravel the complex history of the lithospheric mantle underneath the Kaapvaal craton. By applying the Os, Hf, Nd and Sr isotope systems to the same sample set, our overarching goal is to arrive at a better understanding of the nature of the events recorded by these rocks.

2. Geological setting and overview of Finsch peridotites

The oldest crust formation in the Kaapvaal craton of southern Africa occurred at ca. 3.6–3.7 Ga, and is represented by gneiss complexes in the Swaziland-Barberton area (e.g. Compston and Kroener, 1988; Poujol et al., 2002). Two main building blocks of the craton, the Witwatersrand block (East) and the Kimberley block (West) (Fig. S1) evolved separately, until their amalgamation at 2.88 Ga (Schmitz et al., 2004). This was followed by Ventersdoorp magmatism at 2.8–2.6 Ga and later by the intrusion of the 2.05 Ga old Bushveld complex (Thomas et al., 1993). The periphery of the Kaapvaal craton was reworked along its west–southwest margin between 1.8 and 2.1 Ga during the Kheis Magondi orogeny (e.g. Alterman and Hölbich, 1991) and along its southern margin between 1.2 Ga and 0.9 Ga during the Khibaran orogeny, forming the Namaqua–Natal unit (e.g. Thomas et al., 1993).

The Group II Finsch kimberlite erupted 118 ± 2.2 Ma ago near the west margin of the Kimberley block (Smith et al., 1985) and transported lithospheric mantle xenoliths to the surface. The Finsch peridotites
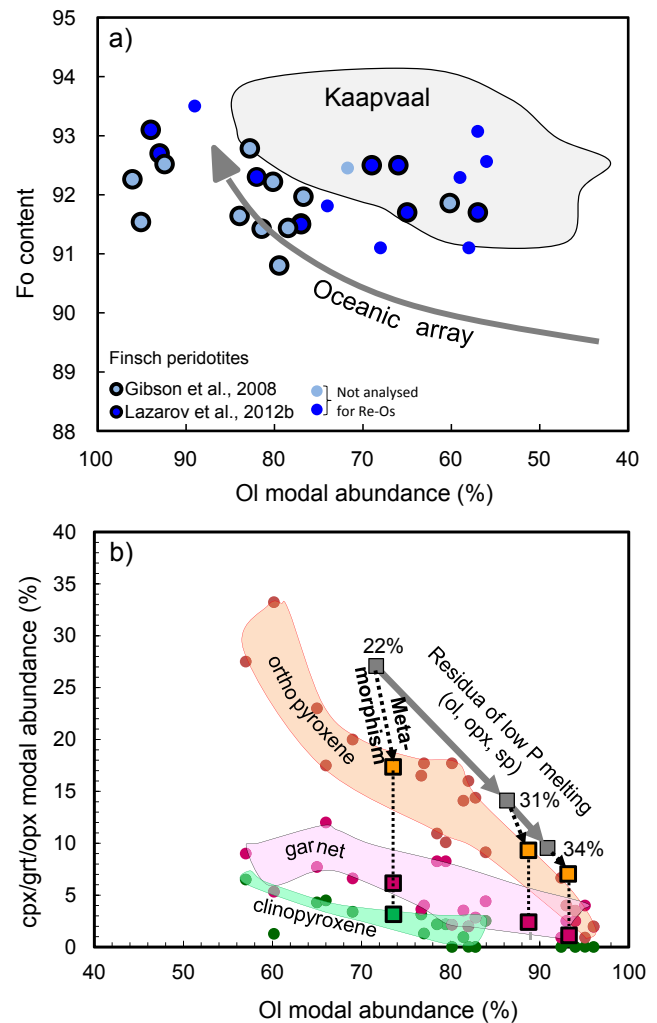
Fig. 1. a) Fo-content in ol versus its modal abundance in Finsch peridotites with data taken from Gibson et al. (2008) (light blue dots) and Lazarov et al. (2012b) (dark blue dots). Samples selected for Re-Os isotope analysis (Table 1) are highlighted by thick black rings. The "oceanic melting array" after Boyd (1989) and the general field for garnet peridotites from the Kaapvaal craton are shown for comparison (data from Hawkesworth et al., 1983; Boyd and Mertzman, 1987; Boyd 1989; Grégoire et al., 2003; Simon et al., 2007). b) Diagram of cpx/grt/opx modal abundances plotted against the modal abundance of ol in Finsch peridotites as taken from Gibson et al. (2008) and Lazarov et al. (2012a). The green circles represent cpx, red circles grt and ocher circles opx modal abundances. Grey squares and arrows represent the trend of residual opx-ol pairs from selected experiments at 1.5 GPa by Falloon et al. (1999); these were normalized to 100% for varying degrees of partial melting (22%, 31% and 34%) at 1.5 GPa. We calculated the bulk composition of the residues from the ol and opx compositions and their proportions as given by Falloon et al. (1999). These residues were recalculated by mass balance to a high-pressure phase assemblage using the mineral compositions of either a cpx-free or a cpx-bearing garnet peridotite from Finsch. The colored squares represent the calculated proportions of opx (ocher), grt (red) and cpx (green) relative to ol. They thus show the modal mineral abundances in residual garnet peridotites at the *P-T* conditions prevailing at Finsch before metasomatism. (For interpretation of the references to colour in this figure legend, the reader is referred to the web version of this article.)

were selected for our study because, as noted by Gibson et al. (2008) and Lazarov et al. (2012b), a major proportion of them follows the "oceanic melting trend" of Boyd (1989) and does not plot into the more orthopyroxene (opx)-enriched Kaapvaal field defined by this author (Fig. 1a). The Finsch peridotites thus comprise some of the least orthopyroxene-rich peridotites sampled from the Kaapvaal craton and

Table 1
Modal composition of Finsch peridotites, contents of selected major elements and calculated degrees of partial melting.

Rock type	Sample	Modal mineral content (%)					Mg#	CaO	Al$_2$O$_3$	Cr$_2$O$_3$	TiO$_2$	partial melting	reference
		ol	opx	cpx	grt	others	ol	(wt%)	(wt%)	(wt%)	(wt%)	(vol%)	
harzburgite	F05 JM2	79.5	10.1	2.2	8.3	sulfide phlog	90.8	0.90	1.80	0.37	0.05	21	Gibson et al., 2008
harzburgite	F05 JM4	60.2	33.2	1.3	5.3	sulfide	91.9	0.78	1.23	0.43	0.02	26	
dunite	F05 JM5	95.1	0.9	0.01	4.00		91.5	0.36	0.52	0.63	0.03	32	
harzburgite	F05 JM6	78.5	10.9	2.2	8.3	sulfide phlog	91.4	1.29	1.36	0.33	0.03	27	
harzburgite	F05 JM7	81.4	14.1	1	3.5		91.4	0.49	0.79	0.28	0.03	27	
harzburgite	F05 JM8	82.8	14.4	–	2.8		92.8	0.31	0.55	0.34	0.01	39	
harzburgite	F05 JM9	92.4	6.7	–	0.9		92.5	0.11	0.18	0.20	0.02	39	
dunite	F05 JM10	83.9	9.1	2.5	4.4	sulfide phlog	91.6	0.77	0.96	0.31	0.04	29	
harzburgite	BD3692	76.7	16.5	3.1	3.6	sulfide phlog	92.0	0.88	1.03	0.24	0.04	28	
harzburgite	BD3694	80.2	17.7	–	2.2		92.2	0.28	0.47	0.28	0.01	35	
dunite	BD3695	96.1	2	–	2	phlog	92.2	–	–	–	–	–	
dunite	F-2	94	3.5	–	2.5		93.1	0.19	0.48	0.24	0.01	42	Lazarov et al., 2012b
harzburgite	F-6	65	23	4.3	7.7		91.7	1.52	1.63	0.62	0.03	24	
dunite	F-8	93	4	0.5	2.5		92.7	0.29	0.51	0.22	0.03	38	
harzburgite	F-9	82	16	0.01	2	sulfide	92.3	0.26	0.36	0.28	0.02	34	
harzburgite	F-11	77	17.7	1.3	4		91.5	0.56	0.86	0.38	0.03	27	
harzburgite	F-12	69	20	3.4	6.6	rutile, sulfide	92.5	1.15	1.45	0.54	1.10	32	
harzburgite	F-15; F15A	66	17.5	4.5	12	sulfide	92.5	1.82	2.63	0.29	0.01	28	
lherzolite	F-16	57	27.5	6.5	9	sulfide	91.7	1.05	2.26	0.43	0.06	20	

Phlogopite is always secondary, sitting in sieve-textured cpx rims and along kelyphite rims; F15 and F15A are two polished slabs from the same sample.

may therefore retain a record of their original petrogenetic history (Gibson et al., 2008). The suite of peridotite xenoliths from the Gibson et al. (2008) and Lazarov et al. (2012a,b) collection selected here for Re-Os, Lu-Hf, Sm-Nd and Sr isotope analysis includes 5 dunites (two with < 2.5 vol% clinopyroxene (cpx) + grt and three with grt only), 11 garnet harzburgites (one with rutile and two cpx-free) and one garnet lherzolite (Table 1; IUGS nomenclature). The garnets from the cpx-free peridotites are termed "subcalcic" thereafter because their composition is not buffered by the coexistence of opx and cpx. The petrology and mineral major and trace element geochemistry have been well characterized in prior studies (Gibson et al., 2008; Lazarov et al., 2012a,b). A summary of the key petrologic features is given in Table 1 and in a brief description below.

Modal abundances of the silicate minerals were determined by using (i) image analysis software on both thin sections and hand specimens (Gibson et al., 2008) and (ii) point counting through transparent mm paper laid over thin sections and large slabs cut from the xenoliths (Lazarov et al., 2012a). The results of these authors show that modal olivine (ol) in the Finsch peridotites ranges from 57 to 96 vol% and opx from 1 to 33 vol%. Modal grt is variable, ranging from 1 to 12 vol%, and cpx modal abundances are generally < 4 vol% with only one peridotite containing 6.5 vol%. Based on these abundances and the major and trace element compositions of the constituent minerals bulk rock compositions were calculated by these authors. A comparison of the compositions calculated by Gibson et al. (2008) and Lazarov et al. (2012a) with the bulk rock XRF analyses of Finsch peridotites (summarized by Griffin et al. (2004) from earlier work) in oxide variation diagrams (electronic supplement, Fig. S2) gives similar correlations for both data sets. There are no error estimates given on the mode determinations by the former authors. Based on the abundance of bulk rock major elements (e.g. Al$_2$O$_3$, SiO$_2$, FeO and MgO) and experimental data of Herzberg (2004), Gibson et al. (2008) estimated that Finsch peridotites experienced between 29 and 39% partial melting beginning at 4.5 GPa and ending at 1.5 GPa. Based on the partitioning of Fe and Mg between olivine and melt and the equations of Frey et al. (1985), Lazarov et al. (2012b) similarly estimated that the Finsch peridotites were residues of between 20 and 42% melting. The estimates from these previous studies are reproduced in Table 1.

The Finsch peridotites have all experienced varying degrees of mantle metasomatism by: (i) silicic melts that have converted olivine to orthopyroxene and (ii) silico-carbonatitic melts/fluids (Gibson al.,

2008; Lazarov et al., 2012b). Lazarov et al. (2009a) obtained a 2.62 Ga Lu-Hf isochron from Finsch subcalcic garnets (from cpx-free harzburgite). When combined with reconstructed lherzolitic bulk rock compositions, a 2.63 Ga isochron arose (Lazarov et al., 2012b). These authors interpreted the isochron as reporting the time of partial melting induced by metasomatism while Shu and Brey (2015) reinterpreted this age as dating the time of metasomatism only. The few bulk-rock Re-Os isotope analyses of Finsch peridotites that have previously been reported in the literature (one sample from Pearson et al., 1995; eight samples from Griffin et al., 2004) yielded a range of T$_{RD}$ ages (rhenium depletion model age assuming no Re in the sample residue) between 1.1 and 2.44 Ga, and T$_{MA}$ ages (Os model age calculated in a similar way to Nd model age) between 1.3 and 4.0 Ga. Further, single-grain Base Metal Sulfide (BMS) analyses by LA-ICP-MS gave T$_{RD}$ ages ranging from 3.2 Ga to highly negative values (Griffin et al., 2004). All model ages from the literature were recalculated in this paper to the PUM model (Meisel et al., 2001; Becker et al., 2006).

The *P-T* conditions of last equilibration of Finsch peridotites were calculated by Gibson et al. (2008) and Lazarov et al. (2009b). Amongst others these authors applied the two-pyroxene thermometer (T_{BKN}) and the Al-in-opx barometer (P_{BKN}) of Brey and Köhler (1990) to cpx-bearing garnet peridotites and the thermometer of O'Neill and Wood (1979) with a correction for Fe^{3+} in grt plus P$_{BKN}$ to cpx-free varieties (Lazarov et al., 2009b). Collectively, most of the equilibrated Finsch garnet peridotites stem from a restricted pressure-temperature range between 5.2 and 6.2 GPa (~160–180 km) and 1150 and 1280 °C. They plot along a cratonic geothermal gradient corresponding to a surface heat flux of ~41 mW/m^2 (Pollack and Chapman, 1977) or ~45 mW/m^2 (McKenzie et al., 2005) and yield a mechanical boundary layer thickness of ~200 km (Gibson et al., 2008).

3. Analytical methods

3.1. Sr, Sm-Nd, Lu-Hf and Re-Os isotope plus HSE determinations (cpx and grt, bulk rock)

Whole-rock Os isotopic compositions and the HSE concentrations for the samples described by Gibson et al. (2008) were obtained at the University of Alberta (Canada) and for those of Lazarov et al. (2012b) at the Freie Universität Berlin (Germany). The samples measured in Alberta were cut into small pieces using a diamond saw and abraded before

crushing them in an agate mortar and pestle. Approximately 1 g of rock powder of each sample was spiked with an appropriate amount of mixed HSE spikes (^{185}Re-^{190}Os-^{191}Ir-^{194}Pt-^{106}Pd). The spike-sample mixtures were digested using inverse *Aqua Regia* in a high-pressure Asher (HPA-S, Anton Paar; P = 130 bar) for ~16 h at ~290 °C. Osmium was extracted from the digestion solution immediately after digestion and the remaining solution was processed for other HSE abundances following the procedure of Pearson and Woodland (2000). Osmium isotope ratios were measured as OsO_3^- using multiple Faraday collectors and amplifiers equipped with 10^{12} Ω resistors on a Thermo Scientific Triton Plus thermal ionization mass spectrometer (TIMS) at the University of Alberta (Liu and Pearson, 2014). Repeated measurements of 1–3 ng loads of the DROsS Os reference solution yielded ^{187}Os/^{188}Os of 0.160948 ± 0.000026 (2σ, n = 15), in good agreement with the value obtained by Luguet et al. (2008) (0.160924 ± 0.000004). The remaining HSE column cuts were measured via peak-hopping SEM on a Thermo Element XR ICP-MS at the University of Alberta. Total procedural blanks were 0.37 pg for Os with ^{187}Os/^{188}Os of 0.16, 4.3 pg for Ir, 19.6 pg for Pt, 17.6 pg for Pd and 0.38 pg for Re. The blank corrections for Os and Ir are negligible (< 0.1% for all samples). The blank corrections of Pt, Pd and Re are variable and slightly higher (Pt 0.4–2.4%; Pd 0.2–2.7%, Re 0.4–5.9%). Fourteen determinations of the OKUM ultramafic reference material spanning the course of this study gave a mean Os concentration of 0.723 ± 0.044 ppb (1SD) and a mean ^{187}Os/^{188}Os = 0.2692 ± 0.0098. This compares well, within uncertainty, to values of 0.749–0.790 pbb Os reported in the literature for this Reference Material (see summary in Chen et al. 2016; no certified value to date) and the Os isotope composition is identical to the ^{187}Os/^{188}Os value of 0.269 reported by Chen et al (2016) – no error given by these authors.

The osmium isotopic compositions and HSE concentrations of the samples analyzed at FU Berlin were digested and analyzed in a similar way using the isotope-dilution technique (Fischer-Gödde et al., 2011). Osmium was also measured by N-TIMS using a Thermo-Finnigan™ Triton and the other HSE were measured by sector-field inductively-coupled plasma mass-spectrometry using Element XR. All data are blank corrected. ^{187}Os/^{188}Os ratios are corrected to a value for the University of Maryland JM Os reference material of 0.11379. Measured ^{187}Os/^{188}Os of the reference material were 0.11379 ± 0.00005 (1SD, Faraday cups) and 0.1141 ± 0.0001 (1SD, SEM, relevant to F15-2 only). The total chemistry blanks are Os = 1 pg with ^{187}Os/^{188}Os of 0.16, Re = 15 ± 5) pg, Ir = 1.3 pg, Ru = 0.8 pg; Pt = 3 pg, Pd = 14 pg. Blank correction on Os is negligible and is on Re between 0.1 and 18.6%. Mean HSE concentrations (± 1SD) of the reference material UB-N (batch c, n = 5) obtained at FUB using the same methods are 3.35 ± 0.10 ng/g Os, 2.90 ± 0.08 ng/g Ir, 6.10 ± 0.23 ng/g Ru, 7.20 ± 0.64 ng/g Pt, 5.79 ± 0.21 ng/g Pd and 0.18 ± 0.02 ng/g Re (For a discussion of heterogeneities within and between different batches of UB-N powder, see Fischer-Gödde et al. (2011). These authors also provide more detailed information on the analytical procedure. Previous work on chondrites has shown that ratios of HSE mass fractions can be reproducible to within a few %, if they were determined by isotope dilution methods (e.g. Horan et al., 2003; Fischer-Gödde et al. 2010). The larger scatter sometimes obtained for mass fractions and ratios in repeat analyses of peridotites reflects heterogeneity of the distribution of different HSE host phases in sample powders (e.g. different sulfides, PGE alloys, selenides, tellurides). For details see the review by Meisel and Horan (2016).

Garnets and clinopyroxenes from eight samples (Table 1) of Gibson et al. (2008) were analyzed for their Lu-Hf and Sm-Nd and five clinopyroxenes for their Sr isotopic compositions at the University of Alberta, following the procedures of Lazarov et al. (2009a) and Shu et al. (2013). Around 10–100 mg of cpx and grt per sample were hand-picked to optical purity under the binocular from the peridotite samples that were crushed in an agate mortar. Grains with spongy rims and visible inclusions (in the transparent grains) were completely removed. To exclude possible grain surface impurities, the separated grains were first leached in 6 M HCl in an ultrasonic bath at room temperature for at least half an hour, washed afterwards in MQ water and finally dried down. After optical inspection the leaching procedure was repeated in 6 M HCl and MQ water when deemed necessary. Before dissolution, the clean mineral separates were spiked with an appropriate amount of Lu-Hf (^{176}Lu-^{180}Hf) and Sm-Nd (^{149}Sm-^{150}Nd); no Rb-Sr spikes were available for spiking the clinopyroxenes. Also, Rb contents are very low in clinopyroxenes and a correction for ^{87}Sr/^{86}Sr is minimal. The Hf–Nd–Sr isotopic compositions were measured by solution-mode multiple collector (MC) ICP-MS on a Thermo Neptune Plus instrument. Total procedural blanks obtained by isotope solution were 18 pg Hf, 5.2 pg Lu, 77 pg Nd and 17 pg Sm. Repeated measurements of the 10 ppb Hf JMC475 standard solution produced ^{176}Hf/^{177}Hf of 0.282152 ± 0.000028 (2SD, n = 10), which is in excellent agreement with the literature (Blichert-Toft et al., 1997; Chu et al., 2002; Pearson and Nowell, 2005). Digestion and analysis of BHVO-1 gave ^{176}Hf/^{177}Hf = 0.283081 ± 0.000015 (2SD), identical to the values reported by Blichert-Toft (2001) and Bizzarro et al. (2003). Repeated measurements of the 25 ppb Nd isotope standard JNdi-1 yielded ^{143}Nd/^{144}Nd = 0.512094 ± 0.000044 (2SD, n = 10), consistent with the accepted values (Tanaka et al., 2000). One analysis of BHVO-1 gave ^{143}Nd/^{144}Nd = 0.512965 ± 0.000017 (2SD). Accuracy and instrument stability for Sr were monitored by repeated measurements of the NIST SRM 987 standard, which gave an average value of ^{87}Sr/^{86}Sr = 0.71026 ± 0.00006 (2SD, n = 3) during the measuring period. This is in good agreement with the recommended value of 0.71034 ± 0.00026 (NIST, certificate issue 1/5/2000). The Sr blanks are estimated to be approximately 4–5 pg and hence insignificant compared to the samples.

3.2. Base Metal Sulfide analyses

We searched for BMS by reflected light microscopy in polished thin sections and polished rock slabs, and identified and analysed them by scanning electron microscopy (SEM), electron microprobe (EPMA) and laser-ablation inductively-coupled mass spectrometry (LA-ICP-MS). The SEM at Universität Frankfurt is a JEOL JSM-6490 equipped with an energy dispersive system (EDS) from Oxford Instruments and the INCA software for quantitative chemical analysis. The major element compositions of the sulfides were determined in Frankfurt by EPMA in wavelength-dispersive mode with a JEOL JXA 8900RL with a focused beam. The acceleration voltage was 20 kV and the beam current 20nA. The counting time was 30–60 s on peak and 15 to 30 s on background (bg) if measured on both sides of the peak (all except Si with 60 s both on peak and bg with one upper bg position). The standards for Fe and S were pyrite, and for Si, Ni, Co and Cu, pure metals were used. Data reduction was carried out by the ZAF procedure.

The HSE concentrations in the various kinds of BMS assemblages were determined at the Arctic Resources Laboratory, the University of Alberta, using a Resonetics Resolution M-50 ArF (193 nm) excimer laser ablation system connected, via Nylon tubing, to a sector-field ICP-MS Thermo Element XR. A detailed description of the method is given in Howarth et al. (2017). The mass resolution was set at (M/ΔM = 300). Samples were ablated for 50 sec in a dual-volume, Laurin-Technic laser cell at a repetition rate of 10 Hz and a laser energy of 1.5–2 J/cm^2. Masses ^{101}Ru, ^{103}Rh, ^{106}Pd, ^{185}Re, ^{191}Ir, ^{192}Os and ^{196}Pt were used for measurement with a dwell time of 10 ms for each element. Sulfide standard La Flamme was used as the calibration standard for the HSE except for Re by NIST glass 610. The very low Cu content in the analysed sulfides resulted in negligible Ar-Cu interference on Rh. Mass ^{57}Fe was used as an internal standard assuming a Fe content of 32 wt% obtained on average for pentlandite by EMPA. The Iolite software was used for data reduction where the time-resolved display allows segment-picking for data evaluation. Howarth et al. (2017) estimate the detection limit to vary in the range between 5 and 10 ppb for the above

elements using 30 s background integrations.

The BMS in the Finsch peridotites are pseudomorphs of the original primary sulfides and consist now mainly of pentlandite and magnetite with rare small copper sulfides (see detailed description below). Individual sulfide grains were too small for LA-ICP-MS. We therefore aimed to obtain bulk BMS compositions that average the phase inhomogeneities and set the laser beam always to a spot size of 90 μm in diameter. It was possible to place one or two such spots onto the larger-sized sulfide blebs and center them onto patches with mainly sulfide while for smaller or elongated sulfides the laser beam ablated the surrounding silicate matrix as well (red circles in Fig. S3). The 32 wt% Fe from pentlandite used as internal standard is probably a minimum value for the Fe-content of the whole mixture of mainly pentlandite and magnetite so that the derived abundances of the HSE are minimum values. The relative abundances, however, should give realistic HSE patterns for the bulk BMS. The silicate matrix surrounding the sulfides contains negligible HSEs so that the derived abundances are minimum values for the bulk BMS for cases where the grain size were smaller than the beam diameter.

4. Results

4.1. BMS and platinum group minerals

4.1.1. Petrography and major element compositions

Finsch peridotites are pervasively veined with serpentine. Olivine, in particular is transected by these veins making it difficult to unequivocally identify (former) isolated BMS inclusions. BMS occur as anhedral roundish, ovoid or edge shaped blebs up to 300 μm in maximum dimension within the serpentine veins where they are most commonly surrounded by olivine (Fig. 2a, c and Fig. S3a–g: electronic appendix). A few ovoid BMS border kelyphite rims of garnets (Figs. 2a and S3e).

BMS also occur as elongated grains (Fig. 2b) or necklaces of irregular streaks within serpentine veins. Irregular elongated grains are also found along grain boundaries between ol and cpx (Fig. S3h) and opx and cpx (Fig. S3i). Almost all BMS blebs and irregular shaped BMS are composite assemblages mainly of pentlandite and magnetite. Rarely, chalcopyrite, bornite, heazlewoodite, pyrrhotite and pyrite are intergrown with pentlandite as found by electron microprobe analysis (Fig. 3 a, b) Pentlandite and magnetite vary in proportion from pentlandite being the dominant phase to a 50:50 mixture. Pentlandite occurs as streaks intergrown with magnetite (Fig. 2 a and S3a, f) in anhedral patches intergrown with magnetite grains (Fig. S3b–e) and as euhedral crystals bordering magnetite intergrowths (Fig. S3g). Magnetite forms anhedral crystals intergrown with pentlandite and also larger patches of finegrained (< 1 μm) intergrowths with a sulfide (Fig. 2c; Fig. S3g). Chalcopyrite was found towards the edges of BMS blebs and as lamellae within pentlandite (Fig. 2d) and also as elongated grains within a serpentine vein (Fig. 1b). According to Lorand and Grégoire (2006) and Lorand and Luguet (2016), for example, the mineral assembles in such complex BMS blebs are the end-products of a series of processes of fractional crystallization from sulfide melts, sub-solidus re-equilibration, serpentinisation and also oxidation. The elongated chalcopyrites and elongated irregular pentlandite necklaces within serpentine veins probably originated during the serpentinisation process. The growth of the BMS along sieve-textured cpx rims could coincide with cpx recrystallisation during the dis-aggregation of the entrained mantle material during transport towards the Earth surface by the host kimberlite.

We obtained 76 BMS analyses by EPMA out of which 65 are pentlandites, 4 are chalcopyrites, others are one monosulfide solid solution (MSS), one pyrite, one pyrrhotite and one bornite and 3 are probably mixed sulfide analyses (Fig. 3 a, b). Representative major element analyses of the Fe, Ni and Cu sulfides are given in Table 2 and all data
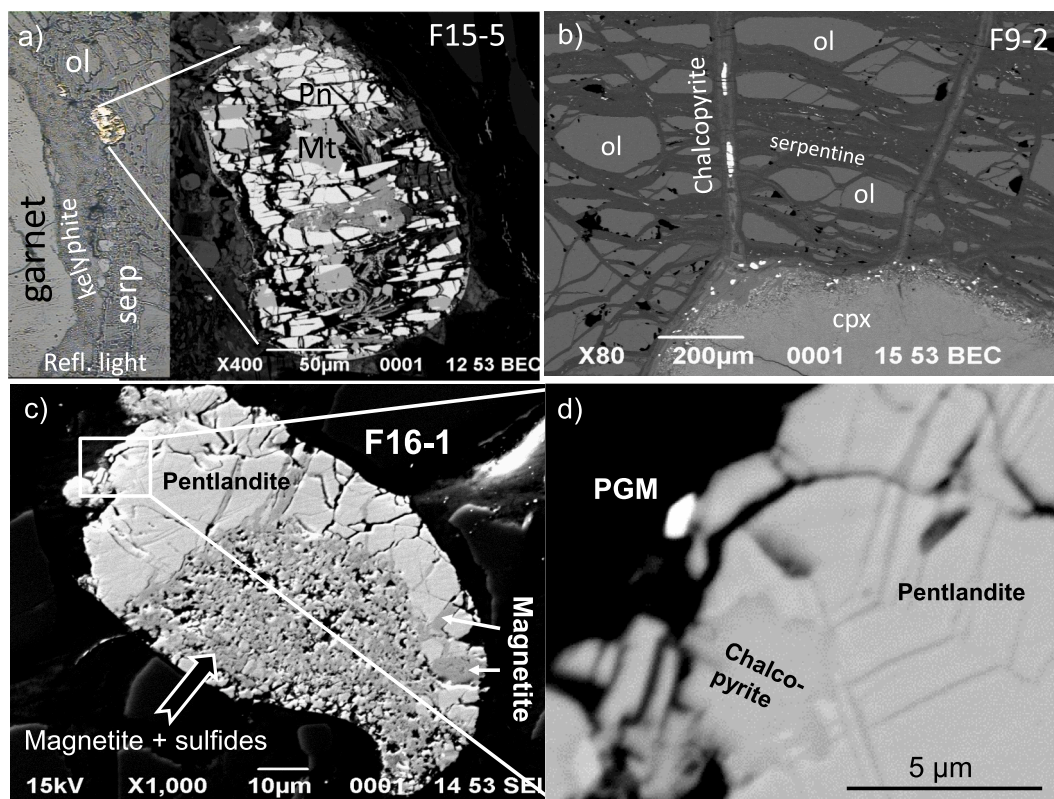
Fig. 2. Reflected light and BSE images of BMS and surrounding silicates. a) BMS bleb in serpentine near kelyphite rim around garnet. The BMS consists of pentlandite streaks intergrown with magnetite. b) Chalcopyrite streaks within serpentine veins in serpentinized olivine. The veins emanate from cpx with a sieve-textured rim. c) BMS bleb consisting mainly of pentlandite and magnetite + sulfide intergrowths within serpentine. The enlargement d) shows a PGM at the rim of the BMS. Pentlandite contains a patch and exsolution lamellae of chalcopyrite.
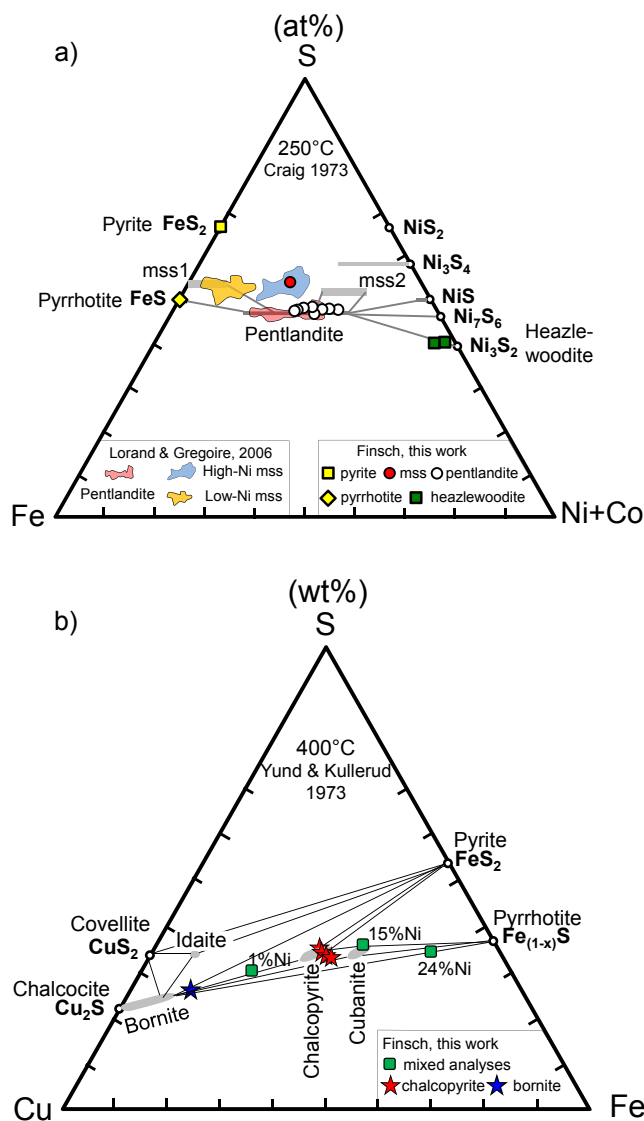
much higher than can be explained as an analytical overlap with BMS. The nugget probably belongs to the group of Os-Ir-Ru arsenic sulfides (osarsite-irarsite-ruarsite) as shown in Table 1a of O'Driscoll and González-Jiménez (2016).

4.1.2. Highly siderophile elements in sulfides

The Finsch peridotite BMS display a range of HSE (including platinum-group elements – PGE – and Re) abundances and IPGE/PPGE ratios [Iridium-group PGE (Ir, Os, Ru) and Platinum-group PGE (Rh, Pt, Pd)]. All analyses together with the grain sizes and form of the BMS are given in Table S2 and a representative selection in Table 3. We display all the data (whole rock and sulfide) as PUM (primitive upper mantle) – normalized patterns, for consistency, and draw the reader's attention to the fact that the difference between PUM and CI-chondrite reservoirs leads to a smoothing of the HSE patterns for PUM normalized compositions. Hence, attention should be paid to the normalization when comparing our whole rock HSE patterns with literature whole rock HSE patterns for cratonic peridotites.

We have distinguished two main groups on the basis of their PUM-normalized patterns (Becker et al., 2006): a major group with (Pt/Ir)$_{PUM}$ < 1 (red patterns in Figs. 4 and S3) and a minor group with fairly flat HSE patterns and (Pt/Ir)$_{PUM}$ ≥ 1 (blue patterns in Figs. 4 and S3). Osmium, Ir and Ru are roughly similar in their PUM normalized relative abundances with 31 of the red patterns being slightly negatively sloped in Os to Ru and seven slightly positively sloped. Osmium to Ru are positively and negatively sloped in about equal proportions for the blue patterns. A number of patterns with (Pt/Ir)$_{PUM}$ < 1 have a trough at Pt only, a feature that is common to many pentlandites and attributed to the coexistence of Pt-rich phases such as the Pt-Bi-Te which were previously identified in BMS from mantle peridotites (see Luguet et al., 2004; Lorand et al., 2010). The others are altogether lower in PUM-normalized PPGE ± Re abundances than the IPGE. The blue (PGE + Re)$_{PUM}$ patterns are either fairly flat or have a slightly positive slope. Three patterns from two samples (Fig. 4e and f) have flat Os, Ir and Ru with low abundances (around 100 × PUM) and about 10 times higher Pt and Pd abundances. Two of the BMS with fairly flat (PGE + Re)$_{PUM}$ patterns occur in serpentinite close to the kelyphite rims of garnets, one at a grain boundary between olivine and clinopyroxene and one is an ovoid BMS in a serpentine matrix. The absolute abundance levels of the HSE in BMS from Finsch lie in the same range as those reported by Aulbach et al. (2004) for isolated sulfide inclusions in xenocrystic olivines and pyroxenes from Canadian (Lac de Gras) kimberlites and from spinel peridotites (e.g. Alard et al., 2011).

4.2. HSE and Re-Os isotopes in Finsch peridotites

Finsch peridotites show variable bulk-rock concentrations of HSEs. For example, Ir ranges from 2.0 to 9.2 ppb and Pd from 0.6 to 9.3 ppb (Table 4). Concentrations of the IPGE (Os and Ir) are similar to, or higher than, the estimates for PUM, and the PPGE (Pt and Pd) are mildly to strongly depleted relative to the IPGE (Fig. 5 a, b). The figure also shows modelling curves by Lorand et al. (2008) for peridotite residues from high degrees of partial melting as a guide. There, Os and Ir have flat to slightly inclined relative abundances and Pt and Pd diminish sharply. Osmium and Ir in the Finsch peridotites have mostly equal PUM-normalized relative abundances (no slope on the PUM-normalized HSE patterns). Osmium is somewhat higher than Ir in only 4 samples. In Fig. 5, the Finsch peridotites are split into two age groups. The older group with Archean T$_{RD}$ ages (2.5–2.7 Ga; Fig. 5a) exhibits strong depletion of the PPGE contents relative to the IPGE ((Pd/Ir)$_{PUM}$ = 0.09–0.27) while this elemental fractionation is less pronounced in the group with post-Archean T$_{RD}$ ages ((Pd/Ir)$_{PUM}$ = 0.36–1; Fig. 5b). The (Pt/Ir)$_{PUM}$ range from 0.13 to 0.82 for the older age group and from 0.38 to 0.8 for the younger group. This elemental fractionation could be interpreted as reflecting a wide range of degrees of partial melting from 10 to 40% with the younger age

Fig. 3. a) a Fe – (Ni + Co) – S phase diagram at 250 °C after Craig (1973) with compositional fields for BMS from the Kaapvaal Craton taken from Lorand and Grégoire (2006) and compositions of BMS from this study (colored symbols). b) a Cu–Fe–S phase diagram at 400 °C after Yund and Kullerud (1966). Colored symbols are our own data; those with annoted Ni contents may be mixed analyses.

documented in Table S1. The pentlandites range in composition from Fe$_{0.37}$Co$_{0.01}$Ni$_{0.62}$ to Fe$_{0.51}$Co$_{0.01}$Ni$_{0.48}$ (Fig. 3a). Individual sulfide blebs are compositionally homogeneous but vary slightly between grains within a sample. They contain up to 1 wt% Co and lie on the Ni-rich side of the compositional range for pentlandites from other peridotite xenolith localities from the Kaapvaal craton (Kimberley, Jagersfontein, Northern Lesotho) given by Lorand and Grégoire (2006). These authors also report compositional fields for Ni-rich and Ni-poor MSS that occur as intergrowths with pentlandite and Cu-rich sulfides in solitary inclusions in silicates from these localities (Fig. 3a).

A 1 μm sized PGE-rich nugget was exposed at the edge of an ovoid sulfide bleb in sample F16 (Fig. 2d). A semiquantitative analysis via EDS gave 3.4 wt% Os, 12.5 wt% Ir, 15.7 wt% Ru, and 4.3 wt% Rh together with 21.7 wt% S, 7.8 wt% As, 3.6 wt% Mg, 2.7 wt% Si, 9.0 wt% Fe, 4.1 wt% Ni, 1.5 wt% Cu (=86.3 wt% in total). The elements Mg and Si and partly Fe, Ni and Cu probably stem from an overlap of the electron beam or of the excitation volume with adjacent silicates and BMS. However, there is no arsenic in these BMS and the S content is

Table 2
Representative electron microprobe analyses of BMS in Finsch peridotites.

Sample	Mineral	Cu (wt%)	S (wt%)	Ni (wt%)	Fe (wt%)	Co (wt%)	Total
F15	Pentlandite	0.02	32.74	35.87	30.29	1.00	99.92
	Bornite	60.32	25.11	0.56	11.59	0.06	97.64
	Chalcopyrite	33.41	34.21	0.25	30.27	0.06	98.19
F9	Pentlandite	0.02	33.25	37.51	28.54	0.54	99.85
	Chalcopyrite	33.28	34.54	0.11	29.54	0.05	97.52
F16	Pentlandite	0.10	33.08	35.77	29.12	0.68	98.76
	Chalcopyrite	32.91	34.65	0.59	29.81	0.08	98.03
F05 JM4	Pyrrhotite	0.01	36.64	0.39	61.73	0.00	98.77
F05 JM 6	Pentlandite	4.33	33.67	34.30	27.21	0.78	100.29
	Pentlandite	n.d.	33.17	37.43	28.49	0.76	99.85
F05 JM 9	Pentlandite	n.d.	33.01	41.31	24.49	0.48	99.29
	Pentlandite	n.d.	33.26	40.53	25.03	0.51	99.33
	Heazlewoodite	n.d.	26.18	70.38	2.00	0.09	98.65
	Pentlandite	n.d.	33.10	37.75	27.29	0.82	98.97
F05 JM 10	Pentlandite	n.d.	33.22	33.14	32.04	0.87	99.27
	Pyrrhotite	0.02	36.96	0.19	62.11	0.01	99.29
	Pentlandite	n.d.	33.34	33.35	31.84	0.74	99.27
	Chalcopyrite	33.91	34.78	0.45	30.08	0.00	99.21
F05 JM2	Pentlandite	n.d.	33.21	38.51	27.83	0.80	100.35
	Heazlewoodite	n.d.	26.89	70.46	3.85	0.13	101.33

Table 3
Representative in-situ HSE analyses of BMS in Finsch peridotites (2SE: within run).

| sample	size, shape of sulfide grain	Os (ppm)	2SE	Ir (ppm)	2SE	Ru (ppm)	2SE	Pt (ppm)	2SE	Pd (ppm)	2SE	Re (ppm)	2SE
F05JM2 − 1	45 × 50 μm, round	0.82	0.10	1.01	0.13	1.94	0.28	0.76	0.17	1.52	0.20	0.30	0.04
F05JM2 − 2	100 × 40 μm, irregular	0.46	0.06	0.46	0.06	1.00	0.12	1.30	0.70	2.33	0.20	0.17	0.02
F05JM2 − 3	75 × 90 μm, round	1.31	0.18	1.49	0.19	3.60	0.42	2.40	1.40	1.78	0.13	0.32	0.04
F05JM2 − 4	120 × 15 μm, vein along the grain boundary	0.25	0.04	0.29	0.03	0.54	0.07	0.09	0.02	0.69	0.07	0.18	0.02
F05JM2-1–1	100 X 150 μm, irregular	0.77	0.05	0.70	0.05	1.78	0.11	0.11	0.02	0.32	0.02	0.19	0.01
F05JM2-1–2		0.26	0.02	0.24	0.02	0.52	0.06	0.09	0.02	0.28	0.04	0.13	0.01
F05JM2-3–1	100 X 20 μm, irregular	0.98	0.06	1.87	0.14	2.36	0.21	0.43	0.06	0.99	0.09	0.63	0.06
F05JM2-5–1	45 × 50 μm, iregular	1.10	0.05	1.32	0.07	2.00	0.13	0.86	0.17	0.65	0.06	0.31	0.02
F05JM2-6–1	20 × 20 μm, round	85.0	18.0	69.0	13.0	92.0	23.0	0.17	0.04	0.28	0.07	0.21	0.06
F05JM2-7–1	60 × 80 μm, round	7.14	0.99	4.89	0.66	13.20	1.70	3.38	0.98	1.57	0.15	0.35	0.05
F05JM2-8–1	100 × 80 μm, round	5.13	0.25	2.97	0.15	5.79	0.34	3.15	0.64	0.61	0.03	0.05	0.00
F05JM4-1–1	60 × 60 μm, round	1710	130	1100	110	1920	150	640	170	33.7	1.60	0.50	0.05
F05JM9 − 1	90 × 80 μm, round	10.40	2.90	7.90	2.20	16.80	4.70	33.00	21.00	22.20	8.20	0.97	0.28
F05JM9 − 5	90 × 100 μm, round	32.18	0.69	27.66	0.64	33.92	0.86	4.69	0.85	3.48	0.15	0.51	0.02
F05JM9 − 6	75 × 25 μm, stripe	2.50	1.10	1.83	0.76	2.90	1.20	0.11	0.08	1.81	0.77	0.03	0.01
BD3692-1–1	110 × 120 μm, round	18.91	0.34	13.20	0.22	23.24	0.44	3.29	0.32	5.35	0.19	0.54	0.02
BD3692-1–2		17.59	0.47	11.29	0.19	18.92	0.43	11.00	2.10	1.54	0.09	0.26	0.01
BD3692-2–1	50 × 70 μm, oval	13.79	0.88	10.29	0.66	15.60	1.20	5.02	1.10	35.00	10.00	0.92	0.08

group showing lower degrees of melting on average. However, the Pd abundances and $(Pd/Pt)_{PUM}$ ratios from 0.5 to 1.3 refute such a simple explanation. They indicate that the HSE abundances and patterns were overprinted subsequent to a partial melting event. PUM-normalized Re contents vary widely from being significantly lower than their respective $(Pd)_{PUM}$ abundance to being more elevated (five samples), with the lowest concentrations being in the samples with older T_{RD} ages.

Nearly all of the Finsch peridotites have lower $^{187}Re/^{188}Os$ (0.012–0.154) and less radiogenic $^{187}Os/^{188}Os$ ratios (0.1096–0.1221) than the primitive upper mantle (PUM, 0.433, and 0.1296 ± 0.008 respectively; Meisel et al. 2001). Two lherzolites (F6 and F12) have higher $^{187}Re/^{188}Os$ values (2.2 and 10.7) and one lherzolite (F05 JM6) has a much more radiogenic Os isotope composition ($^{187}Os/^{188}Os = 0.1822$) (Fig. 6a and Table 4). There is no significant correlation between $^{187}Re/^{188}Os$ and $^{187}Os/^{188}Os$ ratios (Fig. 6a). Of the 19 Finsch peridotites, 10 have Archean T_{RD} model ages (2.5–2.8 Ga), and the remainder have Proterozoic T_{RD} ages (1.0–2.37 Ga; Table 4). In general, Os model ages (T_{MA}) are slightly to significantly greater than T_{RD} ages, with three generating negative values due to extremely high $^{187}Re/^{188}Os$ (F6 and F12) or radiogenic $^{187}Os/^{188}Os$ (F05 JM6). Fig. 6b shows a comparison with the Re-Os isotope compositions of BMS from Finsch xenoliths obtained in-situ by LA-ICP-MS by Griffin et al. (2004). The sulfide data span a very wide

range with more than half of them having isotope ratios above that of PUM. We note that the in-situ method is limited in its application to low Re/Os on BMS due to the isobaric overlap of ^{187}Re and ^{187}Os and, as a consequence, Nowell et al. (2008) recommended a limiting value for $^{187}Re/^{188}Os$ of 0.5 while Rudnick and Walker (2009) point out that even then, the correction factor is 80% on ^{187}Os. We will therefore limit our discussion only to data with $^{187}Re/^{188}Os$ and $^{187}Os/^{188}Os$ ratios below PUM.

4.3. Hf-Nd-Sr isotope compositions of Finsch garnets and clinopyroxenes

The newly measured Hf and Nd isotope ratios of the garnets and clinopyroxenes from eight Finsch peridotites selected from the suite studied by Gibson et al. (2008) are given in Table 5 together with the Sr isotope ratios of clinopyroxenes from five samples. The data are shown in Fig. 7 and in the electronic supplement in Figs. S4 a, b where they are compared to the results of Lazarov et al. (2009a, 2012b). The Lu-Hf as well as the Sm-Nd isotope data for the garnets obtained in this study plot within the range of the data reported by Lazarov and co-workers except for one sample with higher $^{143}Nd/^{144}Nd$ ratios (Fig. 7b). As in Lazarov et al. (2012b), the $^{176}Hf/^{177}Hf$ and $^{143}Nd/^{144}Nd$ ratios of the clinopyroxenes are always slightly less radiogenic than those in the coexisting garnets, resulting in positively-sloped tie lines (Fig. 7). An
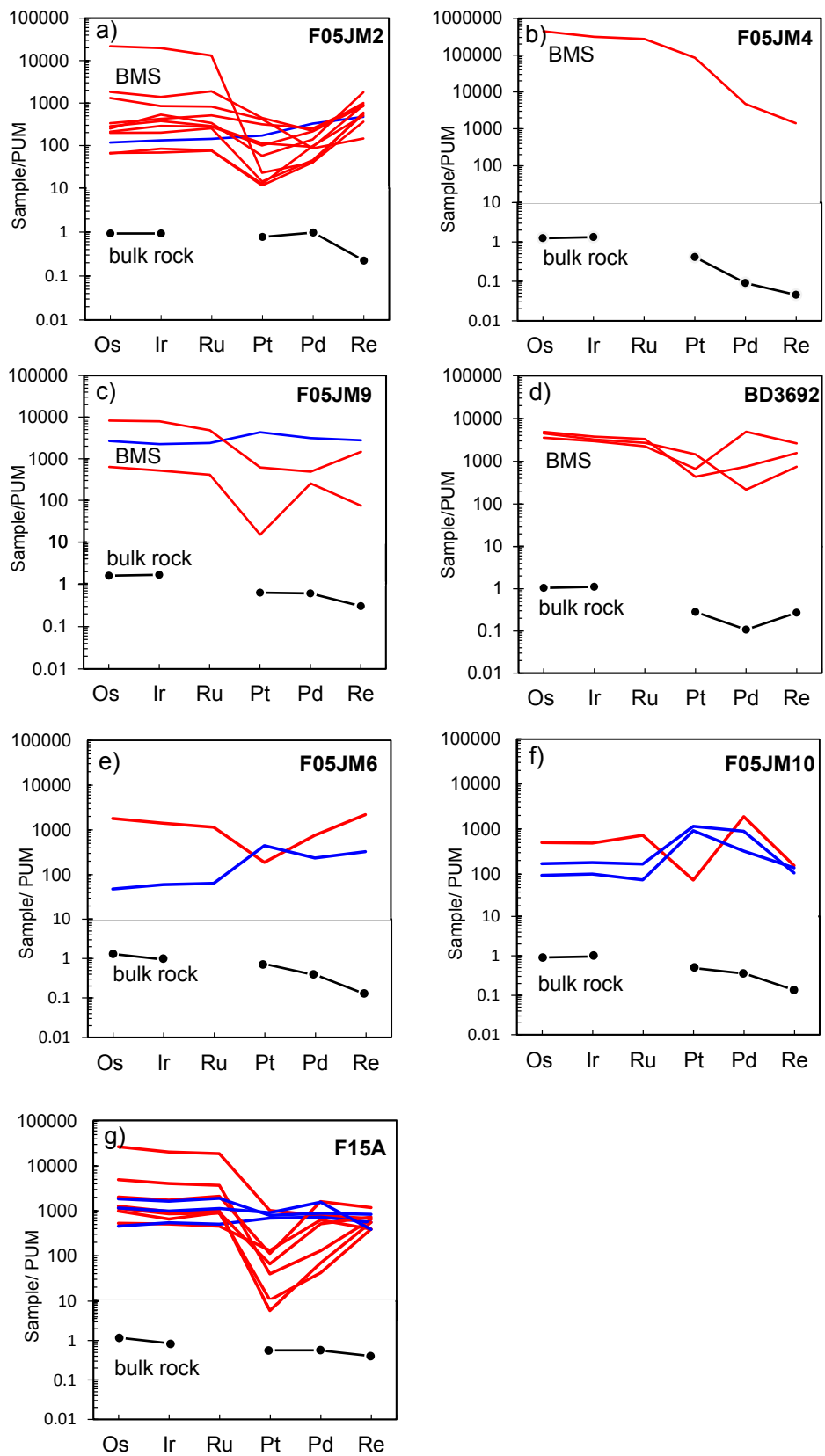
Fig. 4. a – g) Primitive upper mantle (PUM; Becker et al., 2006) normalized HSE patterns of "BMS" from Finsch peridotites and their bulk rock compositions. BMS with $(Pd/Ir)_{PUM} < 1$ are shown in red and with $(Pd/Ir)_{PUM} \sim < 1$ in blue. (For interpretation of the references to colour in this figure legend, the reader is referred to the web version of this article.)

Table 4
Re–Os isotope ratios and HSE concentrations of peridotites from Finsch mine.

sample		weight (g)	Os ppb	Ir ppb	Ru ppb	Pt ppb	Pd ppb	Re ppb	$^{187}Re/^{188}Os$	1 SE	$^{187}Os/^{188}Os$	$^{187}Os/^{188}Os$ (i = 118 Ma)	T_{RD} (Ga) PUM	T_{RD} (Ga) (i = 2.6 Ga) PUM	T_{MA} (Ga) PUM	Pd/Ir	Pt/Ir
Archean age group																	
BD3694		1.002	2.496	2.727		0.809	0.786	0.006	0.012	0.001	0.10961	0.10959	2.71	2.78	2.78	0.29	0.30
F05 JM8		1.002	2.818	2.573		1.760	0.741	0.063	0.107	0.001	0.11045	0.11023	2.63		3.47	0.29	0.68
BD3695		1.001	2.969	2.686		1.232	1.278	0.029	0.048	0.001	0.11050	0.11041	2.60	2.88	2.92	0.48	0.46
BD3692		1.005	4.092	3.906		2.151	0.767	0.095	0.112	0.001	0.11070	0.11048	2.59		3.47	0.20	0.55
*F9		2.028	3.190	2.200	3.230	3.710	0.609	0.050	0.075	0.004	0.11078	0.11063	2.57	3.01	3.10	0.28	1.69
*F8		1.999	4.330	2.730	5.400	2.570	1.570	0.079	0.087	0.003	0.11132	0.11115	2.50	3.02	3.12	0.58	0.94
*F8-2	replicate	1.981	4.610								0.11096	0.11079	2.55				
*F8-3	replicate	2.094	4.000								0.11118	0.11101	2.52				
*F12		2.026	3.250					7.19	10.7	0.004	0.11471	0.09374	2.03		negative		
*F12-2	replicate	2.006	2.600								0.11130		2.49				
*F11		2.034	3.080					0.032	0.050	0.004	0.11147	0.11137	2.48	2.77	2.79		
*F11-2	replicate	2.051	4.090								0.11469		2.03				
F05 JM7		1.000	4.684	4.391		4.853	2.884	0.051	0.052	0.001	0.11195	0.11184	2.41	2.72	2.74	0.66	1.11
F05 JM4		1.002	4.864	4.624		3.118	0.640	0.016	0.016	0.001	0.11261	0.11258	2.31	2.41	2.40	0.14	0.67
*F6		2.044	3.310	2.040	4.280	2.640	1.270	1.53	2.2	0.004	0.11702	0.11702	2.31		negative	0.62	1.29
F05 JM9		1.002	6.252	5.883		4.853	4.355	0.106	0.082	0.001	0.11287	0.11271	2.30	2.78	2.82	0.74	0.82
Post-Archean age group																	
F05 JM10		1.002	3.554	3.392		3.783	2.427	0.044	0.060	0.001	0.11492	0.11481	2.02	2.37	2.33	0.72	1.12
*F2		2.004	4.270	2.720	5.530	4.300	4.010	0.136	0.154	0.003	0.11773	0.11743	1.66	2.57	2.56	1.47	1.58
*F16		2.032	2.440					0.111	0.218	0.005	0.11833	0.11790	1.60	2.89	3.06		
*F16-2	replicate	2.021	2.640								0.11811		1.63				
F05 JM5		1.000	9.191	9.202		12.325	9.347	0.047	0.025	0.001	0.11922	0.11917	1.43	1.58	1.51	1.02	1.34
F05 JM2		1.001	3.642	3.259		5.889	6.940	0.078	0.103	0.001	0.12160	0.12140	1.13	1.74	1.47	2.13	1.81
*F15-2		2.021	3.540					0.250	0.340	0.003	0.12170	0.12103	1.18		5.31		
*F15-1	replicate	2.008	3.880								0.12207		1.13				
F05 JM6		1.001	5.319	3.444	6.510	5.480	2.954	0.045	0.041	0.001	0.18215	0.18207	negative		negative	0.86	1.59

Note: Osmium model ages (T_{RD} and T_{MA}) were calculated based on the primitive upper mantle (PUM) model from Meisel et al. (2001), along with (^{187}Re) = 1.666 × 10−11/year. ($^{187}Os/^{188}Os$)i represents the initial values when the peridotite xenoliths were erupted at 118 Ma using the present-day measured $^{187}Re/^{188}Os$. For samples with $^{187}Re/^{188}Os$ below 0.1, their $^{187}Os/^{188}Os$ ratios were calculated back to the 2.6 Ga age which was derived from the Lu-Hf isotope system for the same sample set. Calculated model ages are given here as T_{RD}(Ga)(i = 2.6 Ga). Sample numbers with * were measured at the Freie Universität Berlin, the other samples were measured in the University of Alberta. The absolute uncertainty of $^{187}Re/^{188}Os$ use 1 SD uncertainties of Re and Os blanks.
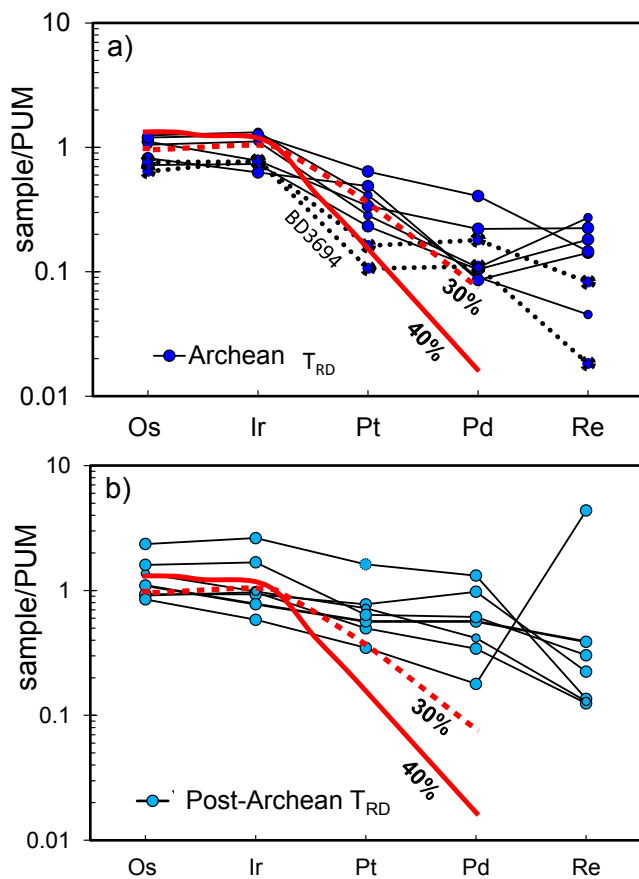
Fig. 5. PUM-normalized HSE patterns of Finsch peridotites separated in two groups of T_{RD} ages a) Samples with Archean T_{RD} model ages and b) samples with Proterozoic ages. The PGE patterns are shown in comparison with residual peridotite patterns calculated for different amounts of partial melting as given by Lorand et al. (2008) and Becker and Dale (2016). The Pt contents in most of our samples and the Pd and Re contents in all samples are elevated compared to these patterns. The exceptions are harzburgite BD3694 and dunite BD3695 (dotted lines).


Fig. 6. a) Variation of $^{187}Re/^{188}Os$ with $^{187}Os/^{188}Os$ in Finsch peridotites. The composition of the primitive upper mantle (PUM) is from Meisel et al. (2001). Shown are our own data and additional whole-rock isotope data from Pearson et al. (1995) and Griffin et al. (2004). b) the same data plus the Re-Os BMS data for Finsch xenoliths from Griffin et al. (2004).

important observation is that all ages of the Lu-Hf grt – cpx tie lines (except for one) for the new samples and those of Lazarov et al (2012b) overlap and are all older (154–668 Ma) than the kimberlite eruption age of 118 ± 2.2 Ma (Smith et al., 1985). For the Sm-Nd isotopes the tie line ages of Lazarov et al. (2012b) coincide, within error, with the kimberlite eruption age while two from the present study are somewhat younger and one is twice as old (the oldest of the Sm-Nd tie line ages).

The $^{87}Sr/^{86}Sr$ ratios of clinopyroxenes in five samples vary between 0.70305 and 0.7065 (Table 5) within the range of clinopyroxenes measured from other cratonic peridotites (see summary in Pearson and Nowell, 2002). These ratios are outside the range of Sr isotopes of their host kimberlite (0.7089 to 0.7106; Fraser and Hawkesworth, 1992) but fall within the compositions defined by Group I kimberlite (Nowell et al., 2004).

5. Discussion

5.1. Formation and metasomatic overprint of sub-cratonic lithospheric mantle beneath Finsch

5.1.1. Partial melting and metasomatism – evidence from major and trace elements, mineral modal abundances

Previous studies have combined chemical parameters, such as the variations of FeO and MgO contents in olivine plus the CaO, Cr_2O_3 and Al_2O_3 contents and HREE patterns of calculated bulk rocks to deduce

the primary melting conditions of the peridotite residues (Gibson et al., 2008; Lazarov et al., 2012b). The main consensus of these two studies are comparable in that: 1) partial melting predominantly occurred at low pressures in the spinel stability field; 2) the extent of partial melting was high and mainly between 30 and 40%; and 3) the 'shallow' melt residues were metamorphosed to garnet peridotites during lithospheric thickening.

A low-pressure origin from melting predominantly in the spinel peridotite stability field is supported further by: (i) a negative, curvi-linear correlation between bulk Yb and bulk Cr_2O_3/Al_2O_3 ratios; and (ii) low to extremely low Yb contents (< 10 ppb) together with extremely high Cr_2O_3/Al_2O_3 ratios (Fig. 8a). The HREE are rapidly depleted in melt residues when garnet is absent (Kelemen et al., 1993; Suhr et al., 1998) while Cr_2O_3/Al_2O_3 increases rapidly with olivine, orthopyroxene and spinel in the residue (Stachel et al. 1998; Canil 2004; Su and Chen, 2018). Brey and Shu (2018) explicitly re-investigated the variation of the Cr_2O_3/Al_2O_3 ratios in residues of both high and low pressures experiments of peridotite melting and the composition of garnets crystallizing from them after metamorphism. They found that garnet-free, low-pressure residua (1–2 GPa) yield a wide variation of Cr_2O_3/Al_2O_3, as observed in Finsch peridotites (Fig. 8a), leading to a wide range of elevated Cr_2O_3 contents in their subsequent metamorphic garnets. Garnet-free, high pressure residua (5 GPa) yield only a very restricted range at low Cr_2O_3/Al_2O_3 ratios (~0.3) and consequently, on metamorphism, can only produce garnets with 1–3 wt% Cr_2O_3. The Cr_2O_3/Al_2O_3 correlation can be modelled as a non-modal batch melting process with ol, opx, cpx and sp in the residue up to 20% melting and with ol, opx and sp at higher degrees of melting (more details in Figure caption 8a). Partition coefficients for Yb were taken from Kelemen et al. (1993) and Suhr et al. (1998) and for Cr and

Table 5

The Lu-Hf, Sm-Nd and Sr isotope compositions of garnets, clinopyroxenes and/or their reconstructed bulk rocks.

sample	$^{176}Lu/^{177}Hf$	error (2 s)	$^{176}Hf/^{177}Hf$	error (2 s)	εHf(0)	$^{147}Sm/^{144}Nd$	error (2 s)	$^{143}Nd/^{144}Nd$	error (2 s)	εNd(0)	$^{87}Sr/^{86}Sr$	error (2 s)
F05 JM2 cpx	0.0006	0.0001	0.283300	0.000008	19	0.189	0.002	0.513119	0.000032	9.4	0.70305	0.00002
F05 JM2 grt	0.067	0.001	0.283492	0.000002	25	0.668	0.007	0.513292	0.000006	12.8		
F05 JM2 bulk rock	**0.057**		**0.283452**		**24**	**0.568**		**0.513256**		**12.1**		
F05 JM6 cpx	0.0007	0.0001	0.283881	0.000075	39	0.053	0.003	0.512277	0.000024	−7.0	0.70591	0.00001
F05 JM6 grt	0.080	0.001	0.284874	0.000007	74	0.265	0.001	0.512780	0.000010	2.8		
F05 JM6 bulk rock	**0.056**		**0.284433**		**59**	**0.220**		**0.512674**		**0.7**		
BD3692 cpx	0.012	0.003	0.284597	0.000003	65	0.131	0.001	0.512567	0.000028	−1.4	0.70650	0.00001
BD3692 grt	0.124	0.034	0.285039	0.000003	80	0.484	0.005	0.512755	0.000012	2.3		
BD3692 bulk rock	**0.054**		**0.284834**		**73**	**0.320**		**0.512668**		**0.6**		
F05 JM5 cpx	0.0013	0.0006	0.282512	0.000023	−9	0.117	0.001	0.512630	0.000026	−0.2	0.70522	0.00002
F05 JM4 grt	0.0116	0.0001	0.282360	0.000002	−17	0.380	0.004	0.512662	0.000027	0.5		
F05 JM7 grt	0.082	0.001	0.285027	0.000004	67	0.424	0.004	0.512858	0.000011	4.3		
F05 JM8 grt	0.035	0.001	0.283870	0.000005	20.801	0.230	0.002	0.512123	0.0	−10.0		
F05 JM10 grt	0.056	0.001	0.283811	0.000003	32	0.552	0.006	0.513143	0.000023	9.9		
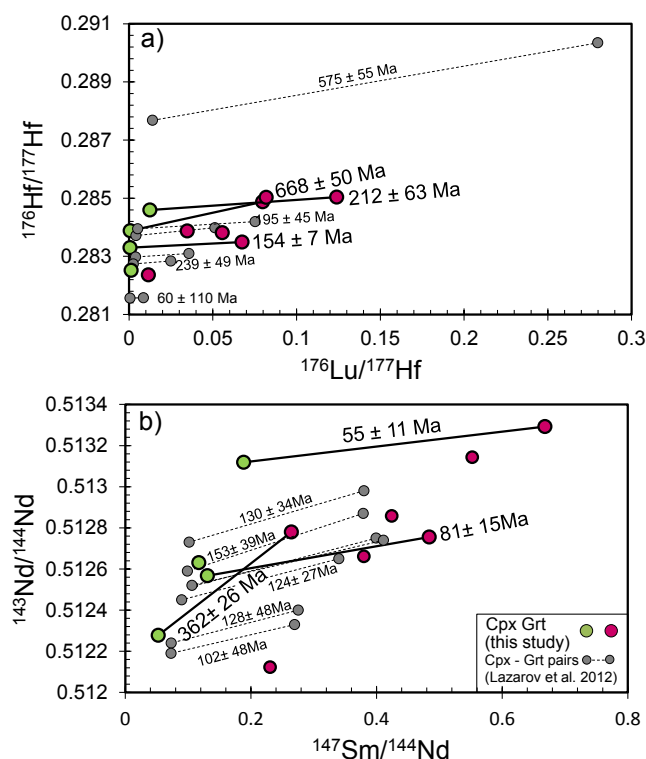
Fig. 7. a) Isotopic compositions of coexisting Finsch garnets and clinopyroxenes shown in a Lu-Hf isochron diagram with data from this study (larger, colored circles) and Lazarov et al. (2012a). Coexisting phases are connected by tie lines. Errors on the ages of the tie lines are derived from the analytical errors. b) The same diagram for the Sm-Nd isotope system.

Al are from Bulatov et al. (2002) for low-pressure (0.75–2 GPa) and Green et al. (2000) and Walter (1998) for high-pressure experiments (3–7 GPa). Based on this modelling, it is obvious that partial melting in the presence of grt fails to reproduce the range and correlation of the varied whole rock major and trace element data from Finsch peridotites (Fig. 8a). Instead, the modelling shows clearly that partial melting at low pressures can reproduce the observed correlation for 15 to 28% melting (Fig. 8a).

We recognize that all the above geochemical parameters contain an element of uncertainty when they are used for either the deduction of the partial melting regime or degrees of partial melting because metasomatism was widespread, and more extensive in some cases, and re-fertilized the Kaapvaal sub-cratonic mantle by partly reintroducing opx, cpx and grt (see in depth discussion by Pearson and Wittig, 2008). In Fig. 1b the modal mineral abundances of Finsch peridotites are shown

together with the variations of mineral modes (ol, opx and small amounts of chromite) produced in the partial melting experiments of Falloon et al. (1999) at 1.5 GPa (grey squares in Fig. 1b). Such residues would be metamorphosed to opx-poorer garnet harzburgites upon lithospheric thickening and equilibration to the final *P-T* conditions recorded by the Finsch peridotites at the time of entrainment: those from 22% partial melting to cpx-bearing and those of 31 to 34% melting to cpx-free garnet harzburgites. The metamorphosed experimental analogues of around 30% partial melting yield ol modal abundances of 89–92 vol%, opx modal abundances of 7–9 vol% and grt of 1–2 vol%. Finsch peridotites are residues after 30–40% of partial melting judging from their olivine chemistry. From the comparison with the modal proportions of the calculated metamorphic equivalents of the low-pressure melting residues it is apparent that most Finsch samples are overabundant in opx, cpx and grt and ol deficient. This indicates that their present opx, cpx and grt modal abundances were mostly elevated via post-melting processes. There are corresponding variations in element abundances and ratios, e.g. an anticorrelation of modal garnet with Yb and Cr_2O_3/Al_2O_3 ratios. Excess grt and cpx contents (besides opx) in residua of extensive melt extraction have been described previously from other localities in the Kaapvaal craton and variously attributed to metasomatism and/or exsolution (Pearson et al., 2002; Simon et al., 2007; Gibson, 2017).

Excess grt in the Finsch peridotites finds its expression in bulk Cr_2O_3 contents higher than the primitive mantle (0.4 wt%; Fig. 8b). Chromium contents higher than the primitive mantle are also observed in other cratonic peridotites (see compilation by Canil (2004). Residues of partial melting at low pressure (i.e. in the spinel stability field) should retain relatively constant Cr_2O_3 at around 0.4 wt% with increasing degrees of partial melting (e.g. Canil, 2004; Brey and Shu, 2018). However, Al_2O_3 is depleted with increasing degrees of partial melting so that the residues with lower Al_2O_3 should yield progressively grt during subsequent metamorphism. At Finsch, the samples with higher bulk Cr_2O_3 than the primitive mantle have the highest modal grt and yet have the lowest Cr_2O_3/Al_2O_3 ratios (Fig. 8c), and a number of them have the highest Yb-contents (Fig. 8a). Excess garnet was reintroduced in these samples by a percolating metasomatic agent (presumably a silico-carbonatitic melt – see below) that is saturated in grt at the *P-T* conditions of metasomatism. Element partitioning between the melt and the crystallizing garnet increases and overprints the original low Yb, and also increases the Cr_2O_3 and Al_2O_3 contents of the depleted residues. In our attempt to constrain the partial melting regime and the degrees of partial melting at Finsch we therefore only consider samples with: (i) low modal grt; (ii) low Yb and (iii) Cr_2O_3 contents between 0.4 and 0.2 wt% (i.e. only within the grey field in Fig. 8d). The non-modal batch melting calculations for Yb and Cr_2O_3/Al_2O_3 ratios above (Fig. 8a) yield degrees of melting from 20 to 28% for these samples.

Obviously, there is some discrepancy between the calculated extent
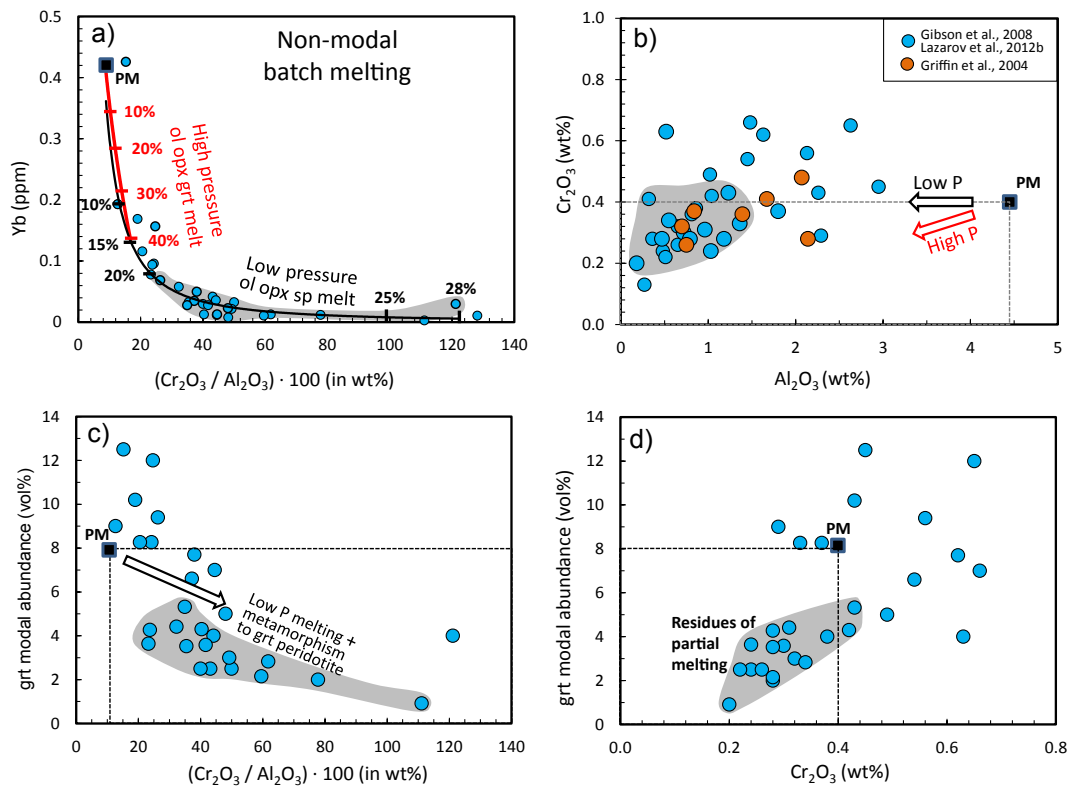
Fig. 8. a) Variation of $(Cr_2O_3/Al_2O_3)\cdot100$ with Yb contents of reconstructed bulk-rock compositions from Gibson et al. (2008) and Lazarov et al. (2012b). The samples plot along a negative, asymptotic trend of decreasing Yb with increasing $(Cr_2O_3/Al_2O_3)\cdot100$ that can be modelled by non-modal batch melting in the spinel stability-field. Melting in the garnet stability only fails to reproduce the trend. Assumed proportions of phases in the spinel stability field were 0.57 ol, 0.235 opx, 0.169 cpx and 0.026 sp in the source with −0.3 ol, 0.4 opx, 0.82 cpx and 0.08 sp contributing to the melt. The source proportions in the garnet stability field were taken as 0.595 ol, 0.19 opx, 0.14 cpx and 0.075 grt with 0.05 ol, −0.15 opx, 1.03 cpx and 0.07 grt contributing to the melt. b) Cr_2O_3 versus Al_2O_3 for the same samples plus bulk rock data from Griffin et al. (2004). Cr_2O_3 remains constant for partial melting in the spinel stability field with increasing degrees of partial melting (black arrow) while it decreases together with Al_2O_3 for melting in the grt stability in a ratio roughly similar to that of the primitive mantle. c) Variation of the modal abundance of grt with Cr_2O_3. The samples within the field outlined by straight lines could represent residues of partial melting. These samples are also outlined in the other figures a, b and d. d) Garnet modal abundances versus $(Cr_2O_3/Al_2O_3)\cdot100$ of reconstructed bulk rocks. The peridotites with the highest and excessive amounts of garnets and elevated Cr_2O_3 contents have the lowest $(Cr_2O_3/Al_2O_3)\cdot100$ ratios.

of partial melting for most Finsch peridotites from their Yb and Cr_2O_3/Al_2O_3 variations (< 28%) and those derived by Gibson et al. (2008) and Lazarov et al. (2012b) from FeO, MgO, CaO and Al_2O_3 compositions (mostly 30–40%). An explanation may lie in the proposal of Gibson et al (2008) that Finsch garnet peridotites are melt residues, that formed when upwelling mantle crosses its solidus at 4.5 GPa and continues to undergo adiabatic melting until 1.5 GPa. When partial melting begins at high pressures with grt as residual phase the partitioning coefficients of Yb, Cr and Al is such that the Yb contents and the Cr_2O_3/Al_2O_3 ratios in the residue initially change only very little while the Mg-value (100·Mg/(Mg + Fe)) increases more substantially. The whole rock FeO and MgO contents record the whole sum of the melting process from high to low pressure while the Yb contents and Cr_2O_3/Al_2O_3 ratios have mainly the memory of melting at lower pressures. The initiation of even "shallow" ridge melting in the Archean would be expected to be considerably deeper than that beneath today's oceanic ridges due to the elevated mantle potential temperature during the Archean (e.g. Herzberg and Rudnick, 2012). The extent of melting estimated by our simple non-modal batch melting calculation is therefore underestimated compared to the modelling with FeO and MgO. The weak correlation of Cr_2O_3 and Al_2O_3 at Al_2O_3 contents less than 1.5 wt% (Fig. 8b) may be the expression of the beginning of melting at high pressures (around 4.5 GPa). Nonetheless, low Yb contents and high to very high Cr/Al ratios unequivocally identify low pressure as the dominating regime for partial melting. This is entirely consistent with numerical models of adiabatic decompression melting.

5.1.2. Evidence from highly siderophile elements in bulk rocks and Base Metal Sulfides

Highly-fractionated PUM-normalized HSE patterns are produced at the high degrees of partial melting that typify cratonic peridotites, most likely due to the incongruent melting of BMS that stabilized PGMs in the residue (Brenan and Andrews, 2001; Pearson et al., 2004). We reproduced in Fig. 5 a, b the PUM-normalized PGE patterns for different degrees of partial melting from Lorand et al. (2008) and Becker and Dale (2016) as a guide to show the behavior of the HSEs in Finsch peridotites. It is apparent from the comparison that the HSE patterns (from Os to Pt) of a number of peridotites from the Archean T_{RD} age group are similar to those expected for very high degrees of melt extraction (30–40%), as expressed by very low $(Pt/Ir)_{PUM}$ ratios down to 0.13. This is consistent with high Fo contents in olivine in these samples and with the partial melting modelling of Gibson et al. (2008) and Lazarov et al. (2012b) based on major elements. At lower degrees of melting residual Pt-rich micro-alloys probably are stable (e.g. Handler et al., 1999; Lorand et al., 1999) and normalized Pt has similar abundance levels as IPGEs. The low Pt abundances (compared to IPGE) again demonstrate the originally high degrees of melting of the Finsch peridotites. This does confirm with other cratonic peridotite localities (e.g. Pearson et al., 2004; Luguet et al., 2015). Also, residues of high degrees of partial melting from other tectonic settings show similarly low Pt e.g. harzburgites and dunites from mantle tectonites [for a summary see Becker and Dale (2016)] and ultra-depleted peridotite xenoliths from New Zealand reported by Liu et al (2015). The latter peridotites have

very low Pt/Ir ratios together with high olivine Fo contents of 92–93.

In the Finsch peridotite suite, there is clear overlap for the IPGE between the calculated HSE-fractionations produced by high degrees of partial melting and the measured patterns (Fig. 5a). Nonetheless, both Pd and Re are too elevated to be consistent with the degree of melting suggested by their Pt concentrations and hence Pd and Re abundances cannot be a result of partial melting alone. The samples in Fig. 5b show a much wider range of IPGE contents with $(Os)_{PUM}$ from 0.8 to 2.4 and overall high (relative to Os and Ir) PPGE. An interpretation of these patterns and abundances as the result of low degrees of partial melting of 10% or less is not consistent with either (i) the Yb contents and Cr/Al ratios or (ii) the depleted major-element composition or high olivine Mg#s of these Finsch peridotites, which requires more than 20% of melting (Table 1; Gibson et al., 2008; Lazarov et al., 2012b). These conflicting signatures signify secondary processes after partial melting and demonstrate that HSEs, as well as the Re-Os isotope system, were disturbed by subsequent metasomatism. The hybrid nature of the HSE patterns and abundances resulting from partial melting and melt/fluid percolation is a common feature of peridotites from the subarctic mantle and also peridotite tectonites from different geodynamic environments (see summary by Lorand et al., 2013, Aulbach et al., 2015; Becker and Dale, 2016).

The PGE-rich nugget found in sample F16 at the edge of a BMS bleb (Fig. 2c, d) is either a residual phase after high degree of partial melting or is a subsolidus exsolution product from a BMS. Luguet et al. (2007) concluded in a study of highly depleted harzburgites where all BMS were consumed by partial melting that PGMs likely account for the whole rock HSE budget. BMS grains are not found in a number of Finsch peridotites (see Table 1), and are particularly absent in cpx-free harzburgite BD3694 and dunite BD3695. These xenoliths have the lowest $(Pt/Ir)_{PUM}$ ratios and their patterns (dotted curves in Fig. 5a) straddle the 40% modelling partial melting curve of Lorand et al. (2008). Luguet et al. (2015) found BMS-free, similarly depleted spinel peridotites from Lethlakane and stated that all BMS were eliminated during high degrees of partial melting likely at low pressures. They interpreted the BMS in the grt- and grt-phlog-peridotites of their sample set to be of metasomatic origin. We cannot make a case on textural grounds that any of the BMS in the Finsch peridotites are residual and assume that all BMS blebs in the olivine and serpentine matrix are of metasomatic origin. This interpretation is consistent with high degrees of partial melting of 30–40% deduced from various geochemical parameters that affected most of the Finsch peridotites, practically consuming all BMS in much of the suite. The PGE composition of the metasomatic sulfide melt should be complementary to residual alloys with their high IPGE/PPGE such that the variously PPGE patterns of the whole rocks are generated during the process. It should therefore have fairly flat or positively sloped PGE patterns.

We assumed in our analytical procedure of HSE by LA-ICP-MS that the large laser beam diameter analysis yields accurate HSE patterns of the bulk BMS. If correct and a representative number of BMS were analyzed, the cumulative proportions should mimic the bulk rock patterns. A comparison of bulk rock with their BMS patterns is made in Fig. 4a–g but is not really conclusive in most cases (exceptions could be BMS poor F05JM4 and BD3692, Fig. 9) because of the relatively small number of BMS that were found and analyzed in polished slabs. The general comparison of the bulk rock HSE patterns (Fig. 5) with those of the BMS shows that the former lack a trough at Pt while a larger proportion of the BMS have a pronounced Pt trough together with (PPGE/IPGE)$_{PUM}$ close to or less than 1 (red patterns in Figs. 4 and S3). Laser ablation analyses on polished mounts or thick sections do not often truly represent the bulk composition of a BMS bleb because the two-dimensional sections may not sample the inhomogeneities within the blebs arising from fractional crystallization, subsolidus exsolution and the serpentinization process. A component complementary to the Pt troughs may be Pt-tellurides or BMS with HSE patterns similar to those of F05JM10 in Fig. 4f, with PPGE strongly elevated relative to IPGEs.

This combination could yield the generally negatively inclined bulk HSE patterns. Comparison of the shapes of melt-depleted HSE patterns (model curves in Fig. 5a, b and the HSE pattern of cratonic peridotite LET28 in Fig. 9a) with the bulk rock HSE patterns of Finsch peridotites suggests that a metasomatic BMS component, with HSE patterns complementary to that of a PPGE depleted bulk-rock pattern must have (PPGE/IPGE)$_{PUM}$ greater than 1 akin to the blue patterns in Fig. 4 (F05JM2, 6 and 9 and F15A). Also, a number of authors (e.g. Luguet et al. 2001; Alard et al. 2011) have established that metasomatic BMS generally have (PPGE/IPGE)$_{PUM}$ greater than 1. We therefore use a BMS from harzburgite F05JM9 (Fig. 4c, blue pattern) as a composition for modelling HSE metasomatism of depleted peridotites in an approach similar to Luguet et al. (2015). However, the HSE abundances of this BMS are fairly high so that we employed the average of the blue patterns in F15A with lower absolute abundances as a second composition. The HSE pattern of a residual peridotite sample from Letseng, Lesotho (LET28; Pearson et al., 2004) was chosen as the end member residue of high-degree partial melting without PPGE disturbance (Fig. 9). To this we added increasing proportions of F05JM9 BMS or the average of F15A BMS. Our model calculations were able to generate the increase of the HSE patterns in all Finsch samples by adding in 0.002–0.09 wt% of a BMS component like that of F05JM9 (Fig. 9a, Table S5). The required amounts are roughly triple for the averaged F15A composition but the patterns generated with this component appear more similar to the patterns of the Finsch peridotites (Fig. 9b, Table S5). Model calculations with a metasomatic agent of higher PPGE/IPGE than F05JM9 BMS and with low to high abundance levels were not successful because of an increase of the PPGEs above the abundance levels of the bulk rocks even for small amounts. The blue patterns with fairly flat PGE appear to more represent the composition of the metasomatizing sulfide melt while the high IPGE abundances of the red patterns are the result of PGE left in the depleted rock as nuggets and their dissolution during the addition of S and PPGE by the metasomatic agent.

The metasomatic history of Finsch peridotites following partial melting is traced via the modal abundances of opx, grt and cpx (Fig. 1b), the bulk rock Cr-contents and the relationship to grt precipitation, the trace-element patterns in the silicate phases (Gibson et al., 2008; Lazarov et al., 2012a), as well as the incompatible PPGE contents in the bulk rocks. These peridotites also exhibit significant positive correlations of $^{187}Os/^{188}Os$ with i) their Pt/Ir and/or Pd/Ir ratios (Fig. 10a, b) and ii) their grt modal abundances. These in turn are positively correlated with the Pt/Ir ratios (Fig. 10c, d). A correlation between grt modal abundances and Pd/Ir ratios is not evident and may be tentatively explained by a subsolidus redistribution of Pt and Pd between BMS and Pt-rich PGM, e.g. Fonseca et al. (2009). A positive correlation also exists between $^{187}Os/^{188}Os$ ratios (also Pt/Ir ratios) and cpx (not shown) but not with opx.

The incompatible PPGE and Re enrichment, together with a positive correlation of $^{187}Os/^{188}Os$ with Pd/Ir ratios has been noted previously in peridotites from Lesotho and Lethlakane (Botswana) (Pearson et al., 2004; Luguet et al., 2015, respectively). These authors suggested that such correlations are due to the precipitation of Re-rich BMS from a percolating melt at sulfide saturation. It should also be noted that BMS are common inclusions in diamonds and that the carbon for diamonds is considered to be introduced into peridotites by metasomatic processes (e.g. Stachel and Harris, 1997).

We observe here, for the first time in cratonic peridotites, a good correlation between the $^{187}Os/^{188}Os$, Pd(Pt)/Ir ratios and also with grt modal abundances (Fig. 10). This suggests a common history between metasomatic sulfide and grt introduction which implies that PPGE enrichment is intimately connected to the metasomatic silicates such as grt and/or cpx and opx. Similarly, Aulbach et al. (2004) observed a weak covariation of Os abundances and $^{187}Re/^{188}Os$ with the Fo-content of olivine in Lac de Gras peridotites (Canada) that can be interpreted as a co-evolution of metasomatic sulfide and silicate melts. Generating these geochemical correlations requires the action of a
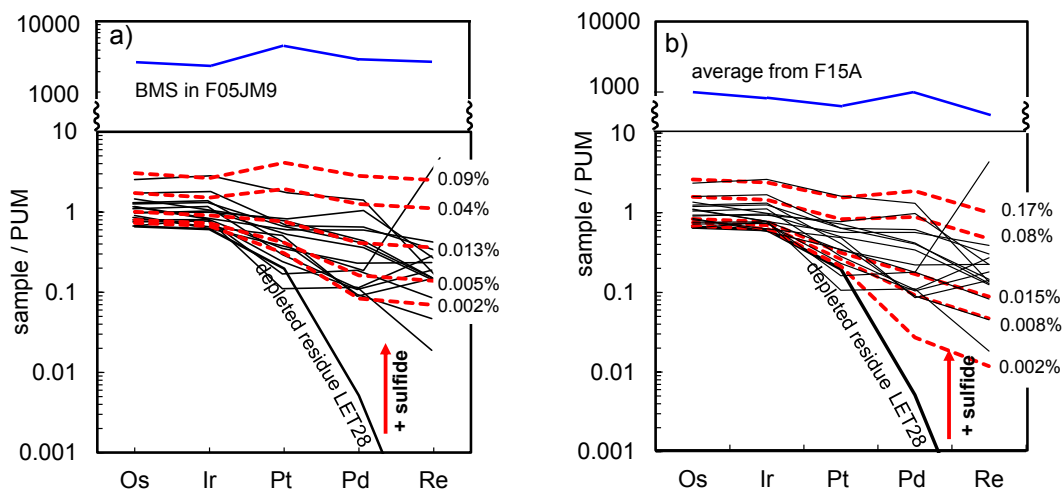
Fig. 9. Modelling of HSE reenrichment in Finsch peridotites. The HSE pattern of a peridotite sample from Letseng (Lesotho; LET28; Pearson et al., 2004) was chosen as an unmodified residue of high degrees of partial melting, metasomatized by increasing amounts of a) the F05JM9 sulfide (Fig. 4c, blue pattern), and b) the average of the blue patterns of peridotite F15A (Fig. 4g) added as model compositions of a metasomatic BMS. Amounts are given in wt%. (For interpretation of the references to colour in this figure legend, the reader is referred to the web version of this article.)

metasomatic agent that contains sufficient sulfur to eventually reach sulfur saturation, has high incompatible lithophile element contents and has the potential to change the silicate mineralogy but does not entirely erase the depleted signature recorded by the major elements.

5.1.3. Nature of the metasomatic agent

Tight constraints on the nature of the metasomatic agent, capable of causing the coupled enrichments that we have observed above, come from the lithophile element isotopic signatures. Shu and Brey (2015) noted that a number of subcalcic garnets (from cpx-free harzburgites)

from the Finsch diamond mine (and other localities on the Kaapvaal craton) possess highly negative εNd and εHf values (down to − 36 and − 66, respectively). Also, the clinopyroxenes from Finsch peridotites have much more radiogenic $^{87}Sr/^{86}Sr$ ratios (0.7030–0.7065; Table 5) than would be expected for long-term depleted residues. These radiogenic Sr isotopic signatures do not stem from the host kimberlite contamination but rather suggest an origin from an old high Rb/Sr reservoir. Garnet inclusions in Finsch diamonds have even more radiogenic $^{87}Sr/^{86}Sr$ ratios and εNd values as low as the subcalcic garnets (Richardson et al., 1984). The highly negative εNd and εHf
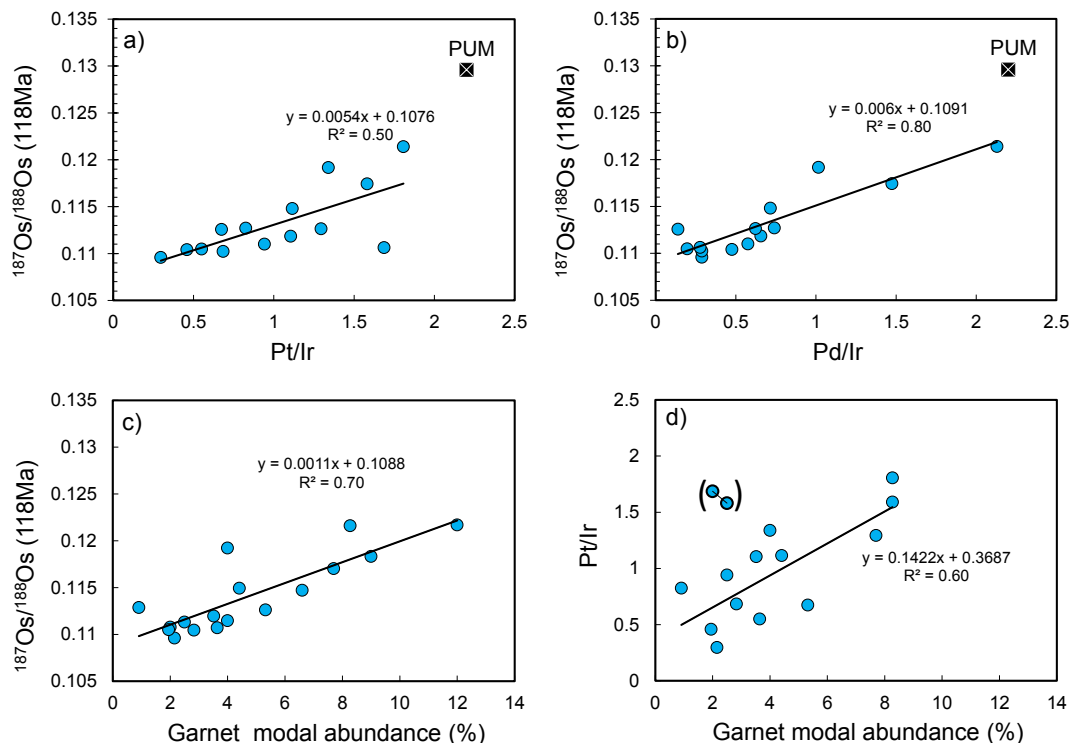
Fig. 10. a – d) Correlations of $^{187}Os/^{188}Os$ ratios with Pt/Ir and Pd/Ir and modal abundances of grt a) The $^{187}Os/^{188}Os$ ratios (calculated back to the time of kimberlite eruption at 118 Ma) are positively correlated with the Pt/Ir ratios of Finsch peridotites. b) The $^{187}Os/^{188}Os$ ratios also increase with increasing Pd/Ir ratios. Pt/Ir and Pd/Ir ratios for the primitive upper mantle (PUM) are from Becker et al. (2006) and $^{187}Os/^{188}Os$ ratio of PUM from Meisel et al. (2001). c) The $^{187}Os/^{188}Os$ ratios are positively correlated with modal grt abundances. d) The Pt/Ir ratios also increase with increasing grt modal abundances. The correlation was calculated without the two data points in parenthesis lying to the upper left above all other data points.

values in some Finsch garnets and pyroxenes indicate that a key metasomatic agent infiltrating the Finsch peridotites contained a middle to early Archean crustal component (Lazarov et al., 2009a; Richardson et al., 1984). We therefore have to identify a metasomatic agent and a process or a continuum of processes that i) leads to the reintroduction of silicate phase(s) and of incompatible elements, without entirely erasing the depleted signature of the major elements; ii) introduces PPGE, Re and radiogenic Os and iii) has an old "crustal" lithophile isotopic signature.

The silica-(opx-) rich nature of many Kaapvaal peridotites and of a number of Finsch peridotites (Fig. 1) led many authors early on to suggest a siliceous melt (fluid) as the metasomatic agent, derived by partial melting from a subducting oceanic plate (e.g. Kesson and Ringwood, 1989; Rudnick et al., 1994; Kelemen et al., 1998). Such an agent, however, cannot fully explain the characteristic features of trace-element patterns in Finsch peridotites: the enrichment in incompatible elements, the relative depletion in HFSE (high field strength elements) and the strong negative Nb-Ta, Zr-Hf and Ti anomalies (Gibson et al., 2008; Lazarov et al., 2012b). Studies by Yaxley et al. (1991) and Rudnick et al. (1992) demonstrated that negative anomalies in HFSE and suprachondritic Zr/Hf ratios, when correlated with sub-chondritic Ti/Eu ratios as observed in the Finsch peridotites and subcalcic garnets, are prime indicators of metasomatism by carbonatitic/kimberlitic melts (Shu and Brey, 2015).

The term "silico-carbonatitic melt" is used here in a generalized way to encompass the products of either near-solidus melting of carbonated peridotite (Wallace and Green, 1988) or the slightly larger melt fractions encompassed by the range of kimberlitic (Dalton and Presnall, 1998) or melilititic (Brey and Green, 1975) melts. In fact, melts of similar bulk composition in this broad spectrum can also be generated by partial melting of carbonated eclogite (Yaxley and Green, 1994) or carbonated pelite (Grassi and Schmidt, 2011a,b; Bulatov et al., 2014). Melts from the latter two sources could clearly generate the ancient "crustal" radiogenic isotope characteristics observed in the Finsch garnets. Silicification of bulk rocks and the growth of grt by such Si-undersaturated and Al-poor compositions is not intuitively obvious but the near-liquidus phases of such melts are opx and/or grt and/or cpx at high pressures (e.g. Wallace and Green, 1988; 1993; Brey and Green, 1975; Dalton and Presnall, 1998; Ulmer and Sweeney, 2002; Girnis et al., 2005). They would precipitate these phases when percolating through and reacting with depleted peridotite wall rock.

Bulatov et al. (2014) and Woodland et al. (2018) have shown by high-pressure experiments with a layered capsule configuration that carbonated and carbon-bearing shales are highly reactive with depleted peridotite. The interaction process starts with the generation of silico-carbonatitic melts in the pelites. These melts act as the transport media to equalize the differences in the chemical potentials of e.g. μSiO_2, μAl_2O_3 and μMgO between the juxtaposed materials. This leads to the growth of opx and grt in the depleted peridotite and the accumulation of residual alkali- and calcium-rich silico-carbonatite melts at the top of the capsules. Percolation of such volatile-rich silico-carbonatitic melts causes further reactions with dry residual mantle by dissolution and reprecipitation leaving a metasomatized peridotite. Because the system now contains volatiles and is above the solidus the reactions continue during the duration of porous flow. The time-integrated melt-rock ratio becomes progressively higher, leading to an increase in the modal abundances of opx, grt ± cpx due to carbonation reactions. Because of the high temperature of the processes, carbonates are not precipitated in the metasomatized peridotite, but the escaping residual melt has a high carbonate activity.

The source region for the metasomatic agent must have radiogenic Os and relatively high PPGE concentrations, so we focus on Archean black shales, with typical examples being from the Barberton greenstone belt. These ancient continental sediments contain carbon, carbonate and sulfur and have trace element inventories derived from mainly two sources (Siebert et al., 2005). One subordinate source

probably is Archean TTG gneisses that provide mainly incompatible trace elements and could be responsible for the highly negative εNd and εHf values in some of the Finsch peridotites. The other trace element flux into these black shales is from komatiites, that provide the highly siderophile elements. The HSE patterns of the Barberton black shales are very similar to those of komatiites due to anoxic weathering in the Archean before the great oxidation event (Siebert et al., 2005). This is consistent with the findings of Gaschnig et al. (2016) that Mesoarchean glacial diamictites (as average of the composition of the upper continental crust) contain a significantly higher mafic component than diamictites from post-Mesoarchean periods, having very high Mg, Ni and Cr and also HSE. In fact, their HSE pattern estimated by Gaschnig et al (2016) for Meso-Archean crust is parallel to HSE patterns from the various units of the Barberton black shales (Siebert et al., 2005).

A melt with a HSE component derived from such black shales or from a Mesoarchean crustal component, that is percolating through depleted peridotite will eventually precipitate HSE bearing BMS when the sulfur saturation point is reached during the course of crystallization and/or by redox reactions. As described in the modeling performed in Section 5.1.2, the BMS compositions with flat PGE amongst the Finsch sulfides, mixed and reacting with residual alloy of a typical PPGE depleted cratonic peridotite composition can satisfactorily explain the entire range of HSE abundances in Finsch peridotites (Fig. 9a, b). The two Finsch peridotite BMS candidates selected have fairly flat HSE patterns compared to those of black shales or of Mesoarchean crust, with their steep positively inclined HSE patterns. Modelling with either black shales or a Mesoarchean crust component as the metasomatic agent was not able to entirely reproduce the PPGE + Re portions of the HSE patterns of the Finsch peridotites. The abundances of Pt and especially Pd and Re rise very quickly and exceed the PPGE + Re contents of the Finsch peridotites even for very small amounts of such a BMS component added. As such, we postulate that if Archean black shale or other Mesoarchean crust component was the metasomatic agent and the Finsch BMS originated by sulfide melt exsolution from percolating silico-carbonatitic melt derived from them, the partitioning of PPGE + Re between the two immiscible melts (immiscible melt in the through-going percolating silico-carbonatitic melt vs. the precipitating sulfide melt) may be such that PPGE + Re abundances are lowered compared to those of the IPGE in the residing sulfide melt, perhaps due to the presence of sulphate in the through-going melt.

The results from the recent high-pressure experimental work on the solubility of sulfur in silico-carbonatite melts (Woodland et al., 2019) show that less than 1 wt% S is dissolved in such melts but several wt% S as sulfate. Such melts are therefore effective for transporting significant amounts of sulfur as a sulfate component through a depleted mantle as long as it is relatively oxidized. However, S saturation is reached almost instantly when a more reducing environment is met. An immiscible sulfide melt will exsolve from the percolating melt upon sulfur saturation, which becomes trapped in a peridotite matrix due to the high dihedral angles of sulfide melts (Ballhaus and Ellis 1996). The silico-carbonatitic melt portion metasomatizes the peridotite minerals cryptically and modally by increasing the modal amounts of garnet and pyroxenes (i.e. because these are the liquidus phases of such melts at high pressures – see above). Also, O'Neill and Mavrogenes (2002) showed experimentally that sulfide saturation in mafic melts depends on the FeO content of the melt. Sulfide saturation in a melt can therefore be reached when its FeO content is lowered by the crystallization of a FeO-rich phase, i.e. garnet. These processes together can explain the co-variation of metasomatic silicate minerals with PPGE contents documented above. They also provide the potential to decouple HSE elemental and isotope systematics from lithophile element abundances and isotope systematics, as often observed in other peridotite suites (Pearson et al., 1995; Aulbach et al., 2015), depending on the scale of observation.

5.2. Timing of melt extraction and metasomatism beneath Finsch

5.2.1. Age constraints from the Sm-Nd and Lu-Hf systems

Bulk-rock compositions of the metasomatized residues of partial melting should form an isochron whose slope could reflect (i) the age of partial melting (if metasomatism has no effect on the system); or (ii) the age of the metasomatic event (if the system is totally re-set) or an errorchron if a mixture of both processes only partially re-set the system during metasomatism. Whole-rock Lu-Hf and Sm-Nd isotope compositions from Finsch were obtained from subcalcic garnets alone (proxies for bulk rock compositions; Lazarov et al., 2009a) or calculated from the modal abundances of grt and cpx (Lazarov et al. 2012b and in this study). The combined old and new Lu-Hf dataset of nineteen Finsch peridotites and subcalcic garnets plot along a 2641 ± 58 Ma isochron that defines a radiogenic initial εHf of +26 (Fig. S4a). One garnet from four other lherzolitic samples measured during this study plots either onto or within error of the 2.64 Ga isochron regression line while the other three plot slightly below. The cpx modal abundances in these three peridotites were very low and no sufficient clean separates could be obtained to perform isotope analyses. Because bulk-rock compositions must lie between grt and cpx (i.e. plot to the left of grt in the isochron diagram) we presume that these samples would also plot on the derived isochron. The 2.64 Ga Lu-Hf isochron age most likely defines the age of major metasomatism of Finsch peridotites. This enrichment event occurred in a mantle that was strongly depleted earlier. The initial εHf value of the isochron is +26 (Fig. S4a), a high value compared to that of a depleted convecting mantle in Neoarchean times (εHf = +8; e.g. Vervoort et al., 1999). However, εHf grows very fast in residues of partial melting (e.g. Bizimis et al. 2003) and residues of high to very high degrees of partial melting in the spinel stability field e.g. at 3.2 Ga (= average of the oldest T_{RD} ages of BMS from Finsch peridotites ; Griffin et al. 2004) should have initial εHf values of +200 or higher (see modelling by Shu and Brey, 2015). The much lower observed initial is therefore more consistent with the isochron line representing a metasomatic event on a highly depleted, at least 3.2 Ga old peridotite endmember (oldest T_{RD} ages from Finsch BMS) and a metasomatizing sediment-derived melt.

For the Sm-Nd isotope system, the combined data set of our study and of Lazarov et al. (2009a and 2012a) yields a considerable spread of $^{147}Sm/^{144}Nd$ and $^{143}Nd/^{144}Nd$ ratios from subchrondritic to suprachondritic with no reliable age information (Fig. S4b), indicating either partial resetting or the effects of subsequent metasomatic processes that disturb the Sm-Nd system but not the Lu-Hf system. Kimberlites have much higher Nd concentrations than Hf (Nowell et al., 2004) and hence minor metasomatism by the host kimberlite melt, or its precursor activity has much more potential to disturb the Sm-Nd isotope system. Preferential disturbance of the Sm-Nd compared to the Lu-Hf isotope system during metasomatic processes in the mantle seems quite universal and has been described already in detail by Bizimis et al. (2003 and 2004)).

5.2.2. Age information from the Re-Os isotope system

All Finsch peridotites except two (F6 and F12) have $^{187}Re/^{188}Os$ ratios < PUM (Fig. 6a), Peridotite F05JM6 has $^{187}Os/^{188}Os$ > > PUM. The larger number of samples show a scattered positive array of data that does not yield an isochron. The oldest T_{RD} age is 2.7 Ga and the mode of ages in a T_{RD} histogram lies at around 2.5 Ga (Fig. 11a). This age has an error of about ± 0.2 Ga and is therefore indistinguishable from the 2.64 ± 0.58 Ga Lu-Hf isochron age.

The range of bulk-rock T_{RD} ages from Finsch peridotites overlap with the T_{RD} ages from the other well-studied localities from the Kimberley block (Newlands and the Kimberley Pool; Menzies et al., 1999; Simon et al., 2007, see summary in Table S3) but the maximum T_{RD} ages from the latter two localities are older (3.2 and 3.0 Ga, respectively) as well as the modes in the age distribution curves (2.7 and 2.8 Ga; Fig. 11a). Hence, it seems likely that the true age of melt

depletion and stabilization of the lithosphere beneath Finsch, and by inference the western block of the Kaapvaal craton, is perhaps several hundred Ma older than the 2.64 Ga Lu-Hf isochron and the mode in T_{RD} ages at 2.5 Ga for the Finsch peridotites studied here. Osmium model ages of up to 3.0 ± 0.2 Ga are produced for some Finsch peridotites when we use the measured Re to correct the ingrown ^{187}Os back to 2.6 Ga (i.e. to the time of main metasomatism) and then calculate a T_{RD} age assuming that the un-metasomatized residue had a Re/Os of zero prior to that time (Table 4).

In-situ laser ablation Re-Os isotope analyses of BMS in Finsch peridotites by Griffin et al. (2004) gave three T_{RD} ages older than any of the bulk rocks up to 3.2 Ga (Fig. 11a). Similarly, Wainwright et al. (2015) found for Lethlakane peridotites (Botswana) that metasomatic BMS can yield T_{RD} ages older than the bulk rocks irrespective of whether they were enclosed in minerals or occurred interstitially. They explained this as the preservation of the Os isotope signature of residual PGMs that were redissolved in the sulfides during metasomatism. There is one PGM at the edge of a sulfide bleb in our Finsch sample suite (Fig. 2d) that may be interpreted as a residual phase. If residual PGMs occur then bulk rock Re-Os isotope analyses constitute a mixture of residual phases and metasomatic BMS and will yield mixed age information. Similarly, if residual PGMs are redissolved in metasomatic BMS, then in-situ Re-Os isotope analyses via LA-ICP-MS will yield T_{RD} ages older than the metasomatic event. Nonetheless, these ages still represent minimum ages. Luguet and Pearson (2019) discussed at length that T_{RD} model ages of BMS in a particular peridotite xenolith suite generally encompass the range of T_{RD} ages from the bulk rocks caused by metasomatism following partial melting. The oldest ages from BMS are probably closest to the partial melting age. For the most depleted peridotites, these BMS ages can closely approximate the bulk rock T_{RD} model ages. The difference between the BMS ages and oldest bulk rock ages diminishes with decreasing fertility of the bulk rock.

Whereas good correlations exist between Os isotope compositions and Pd/Ir plus Pt/Ir ratios and also with grt modal abundances (Fig. 10 a-d), there is no correlation with the Re/Os ratios. As discussed in Section 5.1.2, the PPGE + Re enrichment observed in bulk rock Finsch peridotite compositions was most likely due to the metasomatic re-introduction of 0.002–0.09 wt% of F05JM9 BMS (respectively 0.002–0.17 wt% of F15A BMS; Fig. 9) in conjunction with the introduction of silicates. We explore here further whether these amounts of the same metasomatic BMS can also explain the range of present-day $^{187}Os/^{188}Os$ ratios in the Finsch peridotites. For our modelling, we choose the "initial" $^{187}Os/^{188}Os$ value of 0.108 (T_{RD} = 3.2 Ga) from the correlation with Pd/Ir (Fig. 10b) as the Os isotopic composition at the time of partial melting. The $^{187}Os/^{188}Os$ ratio of the metasomatizing sulfide was set to 0.110, the average of komatiites from the Barberton greenstone belt calculated to an age of 2.6 Ga (Komatii and Weltevreden Formations; Puchtel et al., 2014). Komatiites were suggested by Siebert et al. (2005) as the source of HSE in the Barberton black shales and worldwide in Mesoarchean diamictites (Gaschnig et al., 2016). We constrain the metasomatic event at 2.64 Ga (the Lu-Hf isochron in the same sample suite), then forward-calculated present-day $^{187}Os/^{188}Os$ ratios from ^{187}Re decay for different amounts of sulfide addition for the same increments as shown in Fig. 9. Our calculations can reproduce the whole range of observed whole rock $^{187}Os/^{188}Os$ values after a period of 2.64 Ga, via addition of BMS in amounts varying form 0.002 and 0.09 wt% for F05JM9 BMS or 0.008–5 wt% for average F15A BMS (Fig. 11b, c). The latter number appears excessive and stems from the relatively low Os abundance of the averaged F15A BMS. Adjustment to somewhat higher Re values would quickly lower the percentage value. Nevertheless, the mass fraction of BMS metasomatism lies mainly in the range of 0.009% to 0.02 wt%, depending on the sulfide, to produce the mode in Os isotope ratios that equate to a 2.5 Ga T_{RD} model age mode (Fig. 11b, c).

All these considerations mean that the Re-Os isotope system in whole rock peridotites, while being very effective in documenting the
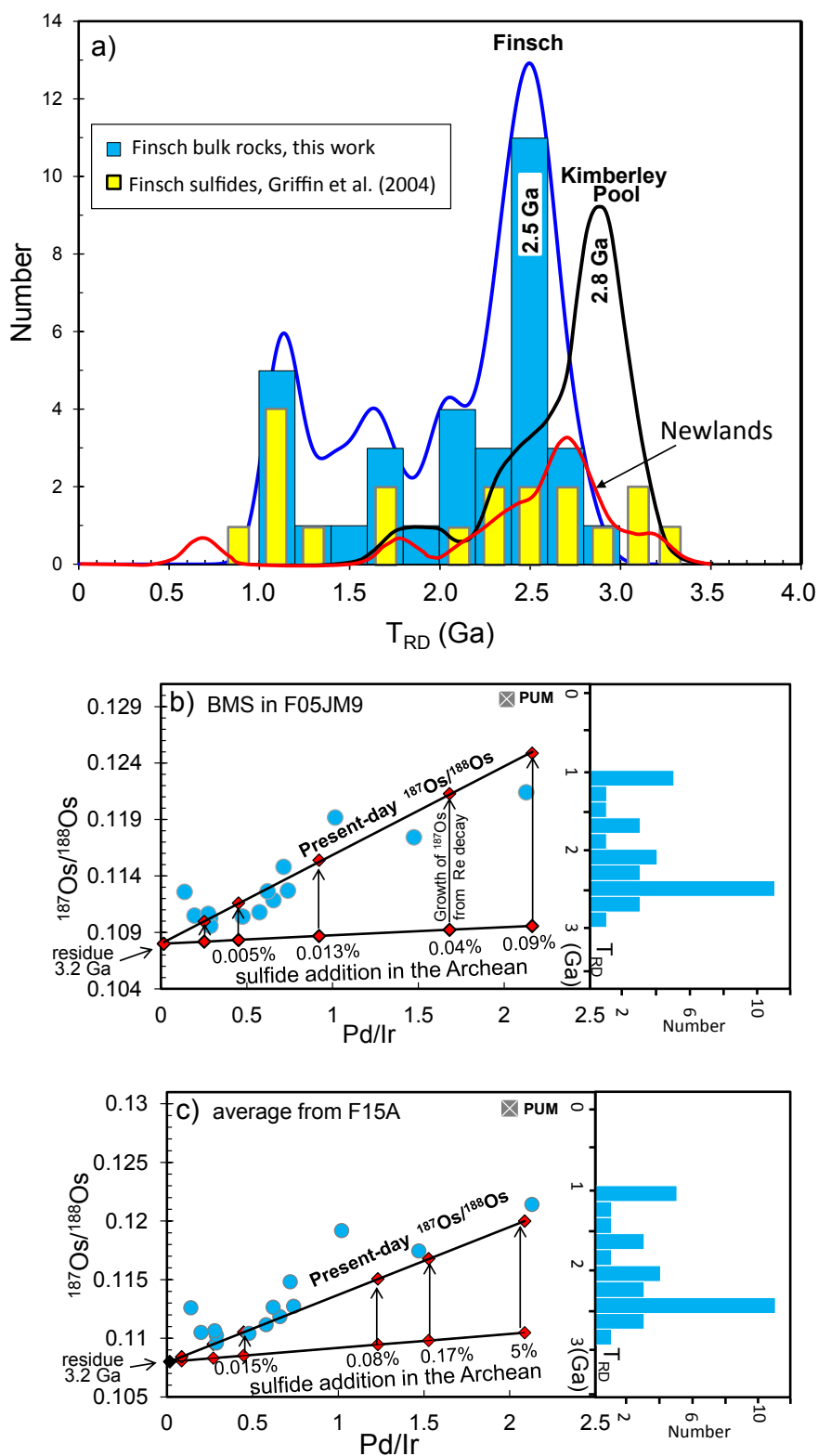
Fig. 11. a) Histogram and probability density curve of T_{RD} ages of Finsch peridotites (data from this study, Pearson et al., 1995; Griffin et al., 2004) together with the probability density curves of T_{RD} ages from Newlands and the Kimberley Pool (Menzies et al., 1999 respectively Simon et al., 2007) and selected Finsch BMS analyses (Re/Os < PUM) from Griffin et al. (2004). The T_{RD} ages of all occurrences are recalculated with the PUM reference model. A pronounced peak at 2.5 Ga is apparent for the Finsch samples. The probability density distribution curve for Kimberley has a mode at 2.8 Ga and for Newlands at 2.7 Ga. b) Modelling of the evolution of $^{187}Os/^{188}Os$ ratios as a function of Pd/Ir ratios arising from increasing amounts of metasomatic BMS added. For our modelling, we choose the intersect $^{187}Os/^{188}Os$ value of 0.108 (T_{RD} = 3.2 Ga) from the correlation with $(Pd/Ir)_{PUM}$ as the value at the time of partial melting. The $^{187}Os/^{188}Os$ ratio of the metasomatizing sulfide was set to 0.110, the average of komatiites from the Barberton greenstone belt calculated to an age of 2.6 Ga (Komatii and Weltevreden Formations; Puchtel et al., 2014). We used a $(Pd/Ir)_{PUM}$ ratio of 0.0076 from LET28 as the ratio of the residue, assumed a metasomatic event at 2.64 Ga and calculated the present day $^{187}Os/^{188}Os$ ratios from the ^{187}Re decay for different amounts of BMS F05JM9 addition for the same increments as in Fig. 9a. The attached histogram is from 11a) but rotated sideways and with T_{RD} ages aligned with the $^{187}Os/^{188}Os$ ratios. The T_{RD} peak corresponds to about 0.007 wt% sulfide added. c) The same modelling as in 11b) only with the average F15A BMS (blue patterns in Fig. 4g). (For interpretation of the references to colour in this figure legend, the reader is referred to the web version of this article.)

Archean provenance of subcratonic lithosphere (e.g. Walker et al., 1989; Carlson and Irving, 1994; Pearson et al., 1995; Luguet and Pearson, 2019), only provides a minimum age for partial melting. The system can be overprinted by the addition of very small amounts of Re during early metasomatism – dominated, at Finsch, in the western Kaapvaal craton, by a major event at 2.64 Ga. This age is well documented by the Hf isotope system and no doubt augmented by other metasomatic events so that even the oldest T_{RD} ages can underestimate the age of partial melting. This interpretation is consistent with recent findings in other cratonic peridotite suites (Wainwright et al., 2015), and not a surprise, as it has been known since the inception of the application of Re-Os dating of peridotites that T_{RD} ages represent minimum estimates for the melting age in any peridotite system (Walker et al., 1989; Pearson et al., 1995; Rudnick and Walker, 2009). Through a multi-isotopic approach, we are able, perhaps for the first time, to place tighter bounds on the likely time difference between melt
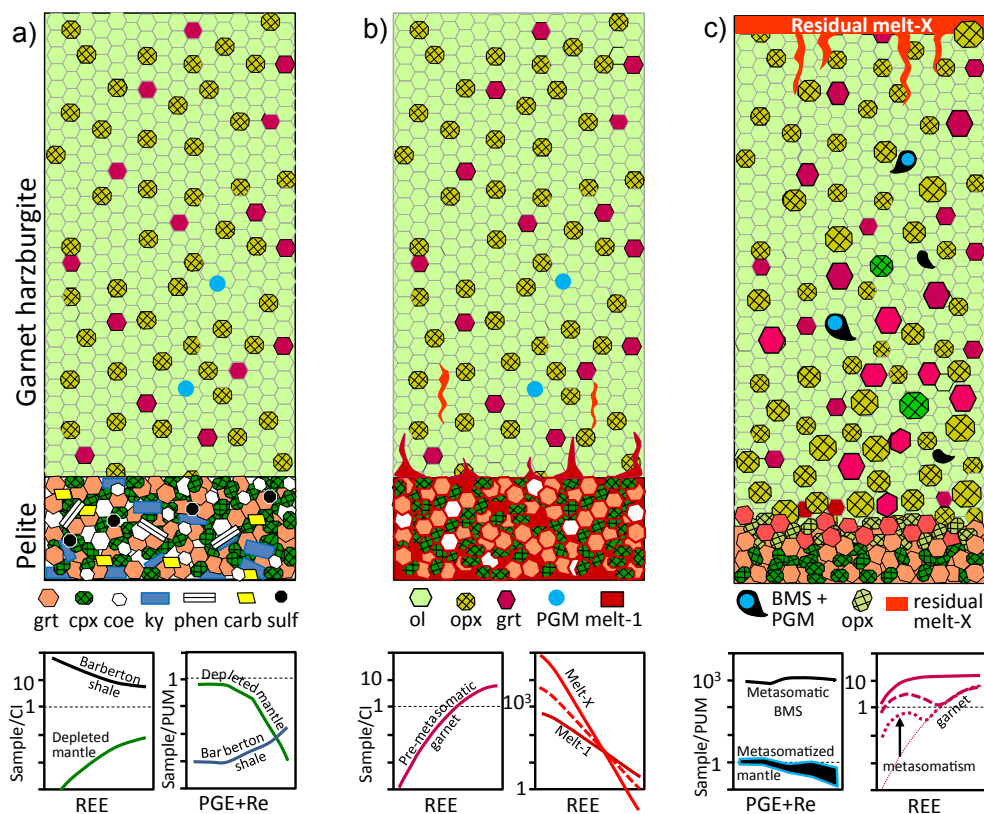
Fig. 12. A sketch of the development of metasomatism by a silico-carbonatitic melt emanating from partially melted carbonated pelite interacting with cpx-free garnet harzburgite. The experimental results of Grassi and Schmidt (2011 a, b) and Bulatov et al. (2014), Brey et al. (2015) and Woodland et al. (2018) are used to represent the evolution of phase assemblages. a) Garnet harzburgite with residual PGMs underlain by a carbonate- and phengite-bearing pelite. Also shown are schematic REE and PGE + Re patterns for these lithologies. The patterns of Barberton shale are after Siebert et al. (2005). b) Melting of pelite and beginning interaction of Melt-1 with harzburgite. The schematic REE patterns of premetasomatic grt in harzburgite and of Melt-1 to Melt-X are also shown. Melt compositions towards Melt-X develop by interaction with peridotite during percolation through the harzburgite column. c) According to the experiments of Bulatov et al. (2014) and Woodland et al. (2018) the sediment layer changes to an eclogitic lithology in the lower part with a garnet-orthopyroxenite above. The garnet harzburgite becomes very rich in opx which decreases in abundance at higher levels in the column. REE grt patterns change from sinusoidal to LREE depleted with increasing amounts of metasomatism. Sulphur is introduced with the melt from the sediment layer. Sulfide saturation in the melt may be reached by fractional crystallization during interaction and/or reduction of sulfate to sulfide. Base metal sulfides may nucleate on or react with residual PGMs.

depletion and metasomatism of sub-cratonic mantle. Specifically, the T_{RD} ages of the Finsch peridotites analyzed here not only mark a minimum time for the initial partial melting event but also may mark or postdate the earliest metasomatism. As such, the main T_{RD} peak at 2.5 Ga from Finsch may rather reflect the main phase of metasomatism that also re-set the Lu-Hf system in many of the samples.

6. Summary and conclusions

Peridotite xenoliths from the Finsch diamond mine (western Kaapvaal craton) show geochemical and petrologic features that are typical of sub-cratonic peridotites, i.e. signatures that suggest they represent residues of extensive melt extraction and subsequent metasomatism. Despite undergoing high degrees of melt-depletion at the time of their formation, the Finsch peridotites exhibit highly variable T_{RD} ages, ranging from the present day to 2.7 Ga with a prominent mode at ~2.5 Ga. This latter age closely overlaps with the metasomatic age determined from a Lu-Hf isochron of 2.641 ± 0.058 Ga, with εHf (t) = +26. This metasomatism is evident from excess modal abundances of opx, grt and cpx in many of the Finsch peridotites compared to those expected for partial melting residues of fertile mantle peridotite. Moreover, we observed for the first time that good positive correlations exist between the modal amounts of garnet and $^{187}Os/^{188}Os$ and Pt/Ir ratios in cratonic peridotites. These correlations suggest that HSE, incompatible trace element re-enrichment and modal metasomatism may result from one single major metasomatic event which disturbed both the Re-Os and Lu-Hf isotope systems. The multi-stage petrological history and geochronological evolution of the Finsch peridotites and, by inference that of the Kaapvaal cratonic root, can be summarized as follows:

1) Highly-depleted peridotitic lithosphere was generated by adiabatic

decompression melting from 4.5 GPa to ~1.5 GPa where melt separated from the depleted residues (Gibson et al., 2008; Lazarov et al., 2012b), possibly around the Mesoarchean (~3.2 Ga). These age constraints are from the oldest T_{RD} ages from BMS of Finsch peridotites (Griffin et al., 2004) and the highly positive initial εHf value (+26) of the 2.64 Ga metasomatic isochron age from Finsch garnet peridotites which pointed to an earlier melt depletion event.

2) The partial melts aggregated, then ascended and subsequently cooled and differentiated in magma chambers to produce oceanic crust. This may have been overlain by oceanic sediments (including black shales).

3) Cratonization by lithosphere thickening (e.g. Wang et al., 2018) would bring packages of oceanic crust and depleted peridotite (harzburgite) to pressures that encompass the 5 to 6 GPa range from where the xenoliths were entrained by kimberlites. We propose that the residual peridotites were metasomatized by fluids or melts emanating from the (altered) oceanic crustal material, including sediment (Fig. 12a; Bulatov et al. (2014) and Grassi and Schmidt, 2011a,b). The subducted portions with low melting components, such as altered seafloor basalts or carbonated and hydrous sediments generate silico-carbonatitic melts (Fig. 12b; Yaxley and Green, 1994; Grassi and Schmidt, 2011a,b; Bulatov et al. 2014). Reactions between these melts and depleted garnet peridotite form orthopyroxene and garnet (Fig. 12b, c; Bulatov et al. 2014). This metasomatism and associated redox reactions may cause reintroduction of BMS in peridotites and the precipitation of diamonds (e.g. Stachel et al., 1998; Shu and Brey, 2015) and modify the REE patterns of garnet (Fig. 12c).

Our detailed study of cratonic peridotites from Finsch highlights the importance of combining information from petrology, major and trace element compositions, Re-Os and Lu-Hf isotope systems and HSE

systematics. This has allowed us to unravel the complex petrological history of the lithospheric mantle beneath the Kaapvaal craton. Ideally, such studies should be supplemented by a detailed investigation of single grain sulfides within individual xenoliths. While only a small subset of our Finsch peridotites permit this, we have shown that, in some cases, even the oldest T_{RD} ages from individual sulfides represent minimum partial melting ages. This is because sulfides are reaction products of metasomatism and retain varying degrees of information about the original melt depletion history of the peridotite. In contrast, the Lu-Hf isotope system can yield isochron ages that can date either partial melting or metasomatic events. The interpretation of Lu-Hf isochrones, however, requires careful examination of the trace and major element compositions in the constituent minerals and a full understanding of the sample history. By combining these approaches, we believe it is possible to impose important constraints on the timescales for melting and metasomatic re-enrichment of cratonic peridotites.

Appendix A. Supplementary data

Supplementary data to this article can be found online at https://doi.org/10.1016/j.precamres.2019.105380.

References

Alard, O., Lorand, J.-P., Reisber, L., Bodinier, J.-M., Dautria, J.-M., O'Reilly, S.Y., 2011. Volatile-rich metasomatism in Montferrier xenoliths Southern France consequences for chalcophile and highly siderophile element abundances in an orogenic-type subcontinental mantle segment. J. Petrol. 52, 2009–2045.

Alterman, W., Hölbich, I.W., 1991. Structural history of the southwestern corner of the Kaapvaal craton and the adjacent Namaqua realm: new observations and reappraisal. Precambr. Res. 52, 133–166.

Aulbach, S., Griffin, W.L., Pearson, N.J., O'Reilly, S.Y., Kivi, K., Doyle, B.J., 2004. Mantle formation and evolution, Slave Craton: constraints from HSE abundances and Re–Os isotope systematics of sulfide inclusions in mantle xenocrysts. Chem. Geol. 208, 61–88.

Aulbach, S., Mungall, J.E., Pearson, D.G., 2015. Distribution and processing of highly siderophile elements in cratonic mantle lithosphere. Rev. Mineral Geochem. 81, 239–304.

Ballhaus, C., Ellis, D.J., 1996. Mobility of core melts during Earh's accretion. Earth Planet. Sci. Lett. 143, 137–145.

Becker, H., Dale, C.W., 2016. Re–Pt–Os isotopic and highly siderophile element behavior in oceanic and continental mantle tectonites. Rev. Mineral. Geochem. 81, 369–440.

Becker, H., Horan, M.F., Walker, R.J., Gao, S., Lorand, J.P., Rudnick, R.L., 2006. Highly siderophile element composition of the Earth's primitive upper mantle: Constraints from new data on peridotite massifs and xenoliths. Geochim. Cosmochim. Acta 70, 4528–4550.

Bizimis, M., Salters, V.J.M., Dawson, J.B., 2003. The brevity of carbonatite sources in the mantle: evidence from Hf isotopes. Contrib. Miner. Petrol. 145 (3), 281–300.

Bizimis, M., Sen, G., Salters, V.J.M., 2004. Hf–Nd isotope decoupling in the oceanic lithosphere: constraints from spinel peridotites from Oahu, Hawaii. Earth Planet. Sci. Lett. 217 (1–2), 43–58.

Bizzaro, M., Baker, J.A., Ulfbeck, D., 2003. A new digestion and chemical separation technique for rapid and highly reproducible determination of Lu/Hf and Hf isotope ratios in geological materials by MC-ICP-MS. Geostand. Geoanal. Res. 27, 133–145.

Blichert-Toft, J., 2001. On the Lu–Hf isotope geochemistry of silicate rocks. Geostand. Geoanal. Res. 25, 41–56.

Blichert-Toft, J., Chauvel, C., Albarede, F., 1997. Separation of Hf and Lu for high precision isotope analysis of rock samples by magnetic sector-multiple collector ICPMS. Contrib. Miner. Petrol. 127, 248–260.

Boyd, F.R., Mertzman, S.A., 1987. Composition and structure of the Kaapvaal lithosphere, southern Africa. In: Mysen, B.O. (ed.) Magmatic Processes: Physicochemical

Principles. Geochemical Society Special Publications 1, 3–12.

Boyd, F.R., 1989. Compositional distinction between oceanic and cratonic lithosphere. Earth Planet. Sci. Lett. 96, 15–26.

Brenan, J.M., Andrews, D., 2001. High-temperature stability of laurite and Ru-Os-Ir alloy and their role in PGE fractionation in mafic magmas. Canadian Mineral. 39, 341–360.

Brey, G.P., Green, D.H., 1975. The role of CO_2 in the genesis of olivine melilitite. Contrib. Mineral. Petrol. 49, 93–103.

Brey, G.P., Köhler, T., 1990. Geothermobarometry in Four-phase lherzolites II. New thermobarometers, and practical assessment of existing thermometers. J. Petrol. 31, 1353–1378.

Brey, G.P., Girnis, A.V., Bulatov, V.K., Höfer, H.E., Gerdes, A., Woodland, A.B., 2015. Reduced sediment melting at 7.5–12 GPa: phase relations, geochemical signals and diamond nucleation. Contrib. Mineral. Petrol. 170, 18.

Brey, G.P., Shu, Q., 2018. The birth, growth and ageing of the Kaapvaal subcratonic mantle. Mineral. Petrol. 112, 23–41. https://doi.org/10.1007/s00710-018-0577-8.

Bulatov, V.K., Brey, G.P., Girnis, A.V., Gerdes, A., Höfer, H.E., 2014. Carbonated sediment–peridotite interaction and melting at 7.5–12 GPa. Lithos 200–201, 368–385.

Bulatov, V.K., Girnis, A.V., Brey, G.P., 2002. Experimental melting of a modally heterogeneous mantle. Mineral. Petrol. 75, 131–152.

Canil, C., 2004. Mildly incompatible elements in peridotites and the origins of mantle lithosphere. Lithos 77, 375–393.

Carlson, R.W., Irving, A.J., 1994. Depletion and enrichment history of subcontinental lithospheric mantle: An Os, Sr, Nd and Pb isotopic study of ultramafic xenoliths from the northwestern Wyoming craton. Earth Planet. Sci. Lett. 126, 457–472.

Carlson, R.W., Pearson, D.G., Boyd, F.R., Shirey, S.B., Irvine, G., Menzies, A.H., Gurney, J.J., 1999. Re-Os systematics of lithospheric peridotites: implications for lithosphere formation and preservation. In: Proceedings 7th International Kimberlite Conference, Red Roof Design, pp. 99–108.

Chen, K., Walker, R.J., Rudnick, R.L., Gao, S., Gaschnig, R.M., Puchtel, I.S., Tang, M., Hu, Z.-C., 2016. Platinum-group element abundances and Re–Os isotopic systematics of the upper continental crust through time: evidence from glacial diamictites. Geochim. Cosmochim. Acta 191, 1–16.

Chu, N.C., Taylor, R.N., Chavagnac, V., Nesbitt, R.W., Boella, R.M., Milton, J.A., German, C.R., Bayon, G., Burton, K., 2002. Hf isotope ratio analysis using multi-collector inductively coupled plasma mass spectrometry: an evaluation of isobaric interference corrections. J. Anal. At. Spectrom. 17, 1567–1574.

Compston, W., Kroener, A., 1988. Multiple zircon growth within early Archean tonalitic gneiss from the Ancient Gneiss Complex, Swaziland. Earth Planet. Sci. Lett. 87, 13–28.

Craig, J.R., 1973. Pyrite-pentlandite assemblages and other low temperature realations in the Fe–Ni–S system. Am. J. Sci. 273-A, 496–510.

Dalton, J.R., Presnall, D.C., 1998. The continuum of primary carbonatitic-kimberlitic melt compositions in equilibrium with lherzolite: data from the system CaO-MgO-Al$_2$O$_3$-CO$_2$ at 6 GPa. J. Petrol. 39, 1953–1964.

Dawson, J.B., 1984. Constraining types of upper-mantle metasomatism? In: Kornprobst, J. (Ed.), Kimberlites II: The Mantle and the Crust-mantle Relationships. Elsevier, pp. 282–331.

Eglington, B.M., Armstrong, R.A., 2004. The Kaapvaal Craton and adjacent orogens, southern Africa: a geochronological database and overview of the geological development of the craton. S. Afr. J. Geol. 107, 13–32.

Falloon, T.J., Green, D.H., Danyushevsky, L.D., Faul, U.H., 1999. Peridotite melting at 1.0 and 1.5 GPa: experimental evaluation of techniques using diamond aggregates and mineral mixes for determination of near-solidus melts. J. Petrol. 40, 9, 1343–1375.

Fischer-Gödde, M., Becker, H., Wombacher, F., 2010. Rhodium, gold and other highly siderophile element abundances in chondritic meteorites. Geochim. Cosmochim. Acta 74, 356–379.

Fischer-Gödde, M., Becker, H., Wombacher, F., 2011. Rhodium, gold and other highly siderophile elements in orogenic peridotites and peridotite xenoliths. Chem. Geol. 280, 365–383.

Fonseca, R.O.C., Campbell, I.H., O'Neill, H.S.C., Allen, C.M., 2009. Solubility of Pt in sulphide mattes: Implications for the genesis of PGE-rich horizons in layered intrusions. Geochim. Cosmoschim. Acta 73, 5764–5777.

Fraser, K.J., Hawkesworth, C.J., 1992. The petrogenesis of group 2 ultrapotassic kimberlites from Finsch Mine, South Africa. Lithos 28, 327–345.

Frey, F.A., Suen, C.J., Stockman, H.W., 1985. The Ronda high temperature peridotite: geochemistry and petrogenesis. Geochim. Cosmochim. Acta 49, 2469–2491.

Gaschnig, R.M., Rudnick, R.L., McDonough, W.F., Kaufman, A.J., Valley, J., Hu, Z.C., Gao, S., Beck, M.L., 2016. Compositional evolution of the upper continental crust through time, as constrained by ancient glacial diamictites. Geochim. Cosmochim. Acta 186, 316–343.

Gibson, S.A., 2017. On the nature and origin of garnet in highly-refractory Archean lithospheric mantle: constraints from garnet exsolved in Kaapvaal craton orthopyroxenes. Mineral. Mag. 81 (4), 781–809.

Gibson, S.A., Malarkey, J.J., Day, J.A., 2008. Melt depletion and enrichment beneath the western Kaapvaal Craton: evidence from Finsch peridotite xenoliths. J. Petrol. 1–36.

Girnis, A.V., Bulatov, V.K., Brey, G.P., 2005. Transition from kimberlite to carbonatite melt under mantle parameters: an experimental study. Petrology 13 (1), 1–15.

Grassi, D., Schmidt, M.W., 2011a. The melting of carbonated pelites from 70 to 700 km depth. J. Petrol. 765–789.

Grassi, D., Schmidt, M.W., 2011b. Melting of carbonated pelites at 8–13 GPa: generating K-rich carbonatites for mantle metasomatism. Contrib. Miner. Petrol. 162, 169–191.

Green, T.H., Blundy, J.D., Adam, J., Yaxley, G.M., 2000. SIMS determination of trace element partition coefficients between garnet, clinopyroxene and hydrous basaltic liquids at 2–7.5 GPa and 1080–1200 ∘C. Lithos 53, 165–187.

Grégoire, M., Bell, D.R., Le Roex, A.P., 2003. Garnet lherzolites from the Kaapvaal craton (South Africa): trace element evidence for a metasomatic history. J. Petrol. 44,

629–657.

Griffin, W.L., Graham, S., O'Reilly, S.Y., Pearson, N.J., 2004. Lithosphere evolution beneath the Kaapvaal Craton: Re–Os systematics of sulfides in mantle-derived peridotites. Chem. Geol. 208, 89–118.

Harte, B., Winterburn, A., Gurney, J.J., 1987. Metasomatic and enrichment phenomena in garnet peridotite facies mantle xenoliths from the Matsoku kimberlite pipe, Lesotho. In: Menzies, M.A., Hawkesworth, C.J. (Eds.), Mantle Metasomatism. Academic Press, London, pp. 145–220.

Handler, M.R., Bennett, V.C., Dreibus, G., 1999. Evidence from correlated Ir/Os and Cu/S for late-stage Os mobility in peridotite xenoliths: implications for Re–Os systematics. Geology 27, 75–78.

Herzberg, C., 2004. Geodynamic information in peridotite petrology. J. Petrol. 45 (12), 2507–2530.

Herzberg, C., Rudnick, R.L., 2012. Formation of cratonic lithosphere: an integrated thermal and petrological model. Lithos 149, 4–15.

Howarth, G.H., Day, J.M.D., Pernet-Fisher, J.F., Goodrich, C.A., Pearson, D.G., Luo, Y., Ryabov, V.V., Taylor, L.A., 2017. Precious metal enrichment at low-redox in terrestrial native Fe-bearing basalts investigated using laser-ablation ICP-MS. Geochim. Cosmochim. Acta 203, 343–363.

Horan, M.F., Walker, R.J., Morgan, J.W., Grossman, J.N., Rubin, A.E., 2003. Highly siderophile elements in chondrites. Chem. Geol. 196, 27–42.

Hawkesworth, C.J., Erlank, A.J., Marsh, J.S., Menzies, M.A., van Calsteren, P., 1983. Evolution of the continental lithosphere: Evidence from volcanics and xenoliths in southern Africa. In: Hawkesworth, C.J., Norry, M.J. (Eds.), Continental Basalts and Mantle Xenoliths. Shiva, Nantwich, pp. 111–138.

Jacobs, J., Pisarevsky, S., Thomas, R.J., Becker, T., 2008. The Kalahari Craton during the assembly and dispersal of Rodinia. Precambr. Res. 160, 142–158.

Jordan, T.H., 1975. The continental tectonosphere. Rev. Geophys. 13, 1–12.

Kelemen, P.B., Hart, S.R., Bernstein, S., 1998. Silica enrichment in the continental upper mantle via melt/rock reaction. Earth Planet. Sci. Lett. 164, 387–406.

Kelemen, P.B., Shimizua, N., Dunnb, T., 1993. Relative depletion of niobium in some arc magmas and the continental crust: partitioning of K, Nb, La and Ce during melt/rock reaction in the upper mantle. Earth Planet. Sci. Lett. 120, 111–134.

Kesson, S.E., Ringwood, A.E., 1989. Slab-mantle interactions 2. The formation of diamonds. Chem. Geol. 78, 97–118.

Lazarov, M., Brey, G.P., Weyer, S., 2009a. Time steps of depletion and enrichment in the Kaapvaal craton as recorded by subcalcic garnets from Finsch (SA). Earth Planet. Sci. Lett. 279, 1–10.

Lazarov, M., Woodland, A.B., Brey, G.P., 2009b. Thermal state and redox conditions of the Kaapvaal mantle: a study of xenoliths from the Finsch mine, South Africa. Lithos 112S, 913–923.

Lazarov, M., Brey, G.P., Weyer, S., 2012a. Evolution of the South African mantle — a case study of garnet peridotites from the Finsch diamond mine (Kaapvaal craton); part 1: inter-mineral trace element and isotopic equilibrium. Lithos 154, 193–209.

Lazarov, M., Brey, G.P., Weyer, S., 2012b. Evolution of the South African mantle—a case study of garnet peridotites from the Finsch diamond mine (Kaapvaal craton); Part 2: multiple depletion and re-enrichment processes. Lithos 154, 210–223.

Liu, J.G., Carlson, R.W., Rudnick, L.R., Walker, J.R., Gao, S., Wu, F.Y., 2012. Comparative Sr–Nd–Hf–Os–Pb isotope systematics of xenolithic peridotites from Yangyuan, North China Craton: additional evidence for a Paleoproterozoic age. Chem. Geol. 332–333, 1–14.

Liu, J.G., Pearson, D.G., 2014. Rapid, precise and accurate Os isotope ratio measurements of nanogram to sub-nanogram amounts using multiple Faraday collectors and amplifiers equipped with 10^{12} resistors by N-TIMS. Chem. Geol. 363, 301–311.

Liu, J.G., Scott, J.M., Martin, C.E., Pearson, D.G., 2015. The longevity of Archean mantle residues in the convecting upper mantle and their role in young continent formation. Earth Planet. Sci. Lett. 424, 109–118.

Lorand, J.-P., Pattou, L., Gros, M., 1999. Fractionation of Platinum-group elements and gold in the upper mantle: a detailed study in Pyrenean orogenic lherzolites. J. Petrol. 40, 957–981.

Lorand, J.-P., Grégoire, M., 2006. Petrogenesis of base metal sulfide assemblages of some peridotites from the Kaapvaal craton (South Africa). Contrib. Miner. Petrol. 151, 521–538.

Lorand, J.-P., Luguet, A., Alard, O., 2008. Platinum-group: a new set of key tracers for the earth's interior. Elements 4, 247–252.

Lorand, J.-P., Alard, O., Luguet, A., 2010. Platinum-group element micronuggets and refertilization process in Lherz orogenic peridotite (northeastern Pyrenees, France). Earth Planet. Sci. Lett. 289, 298–310.

Lorand, J.-P., Luguet, A., Alard, O., 2013. Platinum-group element systematics and petrogenetic processing of the continental upper mantle: a review. Lithos 164, 2–21.

Lorand, J.-P., Luguet, A., 2016. Chalcophile and siderophile elements in mantle rocks: trace elements controlled by trace minerals. Rev. Mineral. Geochem. 88, 441–488.

Ludwig, K.R., 2012. Isoplot 4.15 – A Geochronological toolkit for Microsoft Excel. Berkeley Geochronology Center Special Publicaton No. 5.

Luguet, A., Alard, O., Lorand, J.-P., Pearson, N.G., Ryan, C., O'Reilly, S.Y., 2001. Laser-ablation microprobe (LAM)-ICPMS unravels the highly siderophile element geochemistry of the oceanic mantle. Earth Planet. Sci. Lett. 189, 285–294.

Luguet, A., Behrens, M., Pearson, D.G., König, S., Herwartz, D., 2015. Significance of the whole rock Re-Os ages in cryptically and modally metasomatized cratonic peridotites: constraints from HSE-Se-Te-systematics. Geochim. Cosmochim. Acta 164, 441–463.

Luguet, A., Lorand, J.-P., Alard, O., Cottin, J.-Y., 2004. Multi-technique study of platinum group element systematic in some Ligurian ophiolitic peridotites. In Highly Siderophile Elements and Igneous processes Special Issue (eds. L. Reisberg, J.-P. Lorand, O. Alard and M. Ohnenstetter). Chemical Geology 208, 175–194.

Luguet, A., Shirey, S.B., Lorand, J.-P., Horan, M.F., Carlson, R.W., 2007. Residual platinum-group minerals from highly depleted harzburgites of the Lherz massif (France)

and their role in HSE fractionation of the mantle. Geochim. Cosmochim. Acta 71, 308–3097.

Luguet, A., Nowell, G.M., Pearson, D.G., 2008. ^{186}Os/^{188}Os and ^{184}Os/^{188}Os measurements by NTIMS: effects of interfering element and mass fractionation correction on data accuracy and precision. Chem. Geol. 248, 342–362.

Luguet, A., Pearson, D.G., 2019. Dating mantle peridotites using Re-Os isotopes: the complex message from whole rocks, base metal sulfides, and platinum group minerals. Am. Mineral. 104, 165–189.

McKenzie, D., Jackson, J., Priestley, K., 2005. Thermal structure of oceanic and continental lithosphere. Earth Planet. Sci. Lett. 233, 337–349.

Meisel, T., Horan, M.F., 2016. Analytical methods for the highly siderophile elements. Rev. Mineral. Geochem. 81, 89–106.

Meisel, T., Walker, R.J., Irving, A.J., Lorand, J.-P., 2001. Osmium isotopic compositions of mantle xenoliths: a global perspective. Geochim. Cosmochim. Acta 65, 1311–1323.

Menzies, A.H., Carlson, R.W., Shirey, S.B., Gurney, J.J., 1999. Re–Os systematics of Newlands peridotite xenoliths: implications for diamond and lithosphere formation, Cape Town, 1998. In: Proceedings of the Seventh International Kimberlite Conference. Red Roof Design, Cape Town, South Africa, pp. 566–573.

Nixon, P.H., Boyd, F.R., 1973. Petrogenesis of the granular and sheared ultrabasic nodule suite in kimberlite, in: Nixon, P.H. (Ed.), Lesotho Kimberlites. Cape and Transvaal, Cape Town, pp. 48–56.

Nowell, G.M., Pearson, D.G., Bell, D.R., Carlson, R.W., Smith, C.B., Kempton, P.D., Noble, S.R., 2004. Hf isotope systematics of kimberlites and their megacrysts: new constraints on their source regions. J. Petrol. 45, 1583–1612.

Nowell, G.M., Pearson, D.G., Parman, S.W., Luguet, A., Hanski, E., 2008. Recise and accurate ^{186}Os/^{188}Os and ^{187}Os/^{188}Os measurements by multi-collector plasma ionisation mass spectrometry, part II: laser ablation and its application to single grain Pt–Os and Re–Os geochronology. Chem. Geol. 248 (3–4), 394–426.

O'Driscoll, B., González-Jiménez, J.M., 2016. Petrogenesis of platinum-group minerals. Rev. Mineral Geochem. 81, 489–578.

O'Neill, H.S.C., Wood, B.J., 1979. Experimental-study of Fe-Mg partitioning between garnet and olivine and its calibration as a geothermometer. Contrib. Miner. Petrol. 70, 59–70.

O'Neill, H.S.C., Mavrogenes, J.A., 2002. The sulfide capacity and the sulfur content at sulfide saturation of silicate melts at 1400°C and 1 bar. J. Petrol. 43, 1049–1087.

Pearson, D.G., 1999. The age of continental roots. Lithos 48, 171–194.

Pearson, D.G., Carlson, R.W., Shirey, S.B., Boyd, F.R., Nixon, P.H., 1995. The stabilisation of Archaean lithospheric mantle: a Re–Os isotope study of peridotite xenoliths from the Kaapvaal craton. Earth Planet. Sci. Lett. 134, 341–357.

Pearson, D.G., Irvine, G.J., Carlson, R.W., Kopylova, M.G., Ionov, D.A., 2002. The development of lithospheric keels beneath the earliest continents: time constraints using PGE and Re-Os isotope systematics. Geol. Soc., London, Special Publ. 199, 65–90.

Pearson, D.G., Irvine, G.J., Ionov, D.A., Boyd, F.R., Dreibus, G.E., 2004. Re–Os isotope systematics and platinum group element fractionation during mantle melt extraction: a study of massif and xenolith peridotite suites. Chem. Geol. 208, 29–59.

Pearson, D.G., Nowell, G.M., 2004. Re-Os and Lu-Hf isotope constraints on the origin and age of pyroxenites from the Beni Bousera peridotite massif: implications for mixed peridotite-pyroxenite mantle sources. J. Petrol. 45, 439–455.

Pearson, D.G., Nowell, G.M., 2005. Accuracy and precision in plasma ionisation multi-collector mass spectrometry: constraints from neodymium and hafnium isotope measurements. In: Holland, J.G., Bandura, D.R. (Eds.), Plasma Source Mass Spectrometry, Current Trends and Future Developments. Royal Society of Chemistry, pp. 284–314.

Pearson, D.G., Wittig, N., 2008. Formation of Archaean continental lithosphere and its diamonds: the root of the problem. J. Geol. Soc., London 165, 895–914.

Pearson, D.G., Wittig, N., 2014. The formation and evolution of cratonic mantle lithosphere – evidence from mantle xenoliths. In: Holland, H.D., Turekian, K.K. (Eds.), Treatise on Geochemistry, second ed. Elsevier, Oxford, pp. 254–292.

Pearson, D.G., Woodland, S.J., 2000. Solvent extraction/anion exchange separation and determination of PGEs (Os, Ir, Pt, Pd, Ru) and Re–Os isotopes in geological samples by isotope dilution ICP-MS. Chem. Geol. 165, 87–107.

Pearson, D.G., Nowell, G.M., 2002. The continental lithospheric mantle reservoir: characteristics and significance as a mantle reservoir. Proc. R. Soc., Series A 360, 1–28.

Pollack, H.N., Chapman, D.S., 1977. Regional geotherms and lithospheric thicknesses. Geology 5, 265–268.

Poujol, M., Robb, L.J., Anhaeusser, C.R., Gericke, B., 2002. Geochronological Constrains on the Evolution of the Kaapvaal Craton, South Africa. Economic Geology Research Institute, pp. 33 information circular 306.

Puchtel, I.S., Walker, R.J., Touboul, M., Nisbet, E.G., Byerly, G.R., 2014. Insights into early Earth from the Pt–Re–Os isotope and highly siderophile element abundance systematics of Barberton komatiites. Geochim. Cosmochim. Acta 125, 394–413.

Richardson, S., Gurney, J., Erlank, A., Harris, J., 1984. Origin of diamonds in old enriched mantle. Nature 310, 198–202.

Rudnick, R.L., McDonough, W.F., Chappel, B.W., 1992. Carbonatite metasomatism in the northern Tanzanian mantle – petrographic and geochemical characteristics. Earth Planet. Sci. Lett. 114, 463–475.

Rudnick, R.L., McDonough, W.F., Orpin, A., 1994. Northern Tanzanian xenoliths: a composition with Kaapvaal peridotites and inferences on metasomatic interactions. In: Meyer, L.O. HOA (Ed.), Kimberlites, related rocks and mantle xenoliths. CPRM Spec Pub Jan/94, Brazilia, pp. 336–353.

Rudnick, R.L., Walker, R.J., 2009. Interpreting ages from Re–Os isotopes in peridotites. Lithos 112S, 1083–1095.

Schmidberger, S.S., Simonetti, A., Francis, D., Gariepy, C., 2002. Probing Archean lithosphere using the Lu–Hf isotope systematics of peridotite xenoliths from Somerset Island kimberlites, Canada. Earth Planet. Sci. Lett. 197, 245–259.

Schmitz, M.D., Bowring, S.A., de Wit, M.J., Gartz, V., 2004. Subduction and terrane

collision stabilize the western Kaapvaal craton tectosphere 2.9 billion years ago. Earth Planet. Sci. Lett. 222, 363–376.

Shu, Q., Brey, G.P., 2015. Ancient mantle metasomatism recorded in subcalcic garnet xenocrysts: temporal links between mantle metasomatism, diamond growth and crustal tectonomagmatism. Earth Planet. Sci. Lett. 418, 27–39.

Shu, Q., Brey, G.P., Gerdes, A., Hoefer, E.H., 2013. Geochronological and geochemical constraints on the formation and evolution of the mantle underneath the Kaapvaal craton: Lu-Hf and Sm-Nd systematics of subcalcic garnets from highly depleted peridotites. Geochim. Cosmochim. Acta 113, 1–20.

Siebert, C., Kramers, J.D., Meisel, T.H., Morel, P.H., Nägler, T.F., 2005. PGE, Re-Os, and Mo isotope systematics in Archean and early Proterozoic sedimentary systems as proxies for redox conditions of the early Earth. Geochim. Cosmochim. Acta 69 (7), 1787–1801.

Simon, N.S.C., Carlson, R.W., Pearson, D.G., Davies, G.R., 2007. The origin and evolution of the Kaapvaal cratonic lithospheric mantle. J. Petrol. 48, 589–625.

Smith, C.B., Allsopp, H.L., Kramers, J.D., Hutchinson, G., Roddick, J.C., 1985. Emplacement ages of Jurassic-Cretaceous South African kimberlites by the Rb–Sr method on phlogopite and hole rock samples. Trans. Geol. Soc. South Africa 88, 249–287.

Stachel, T., Harris, J.W., 1997. Diamond precipitation and mantle metasomatism; evidence from the trace element chemistry of silicate inclusions in diamonds from Akwatia, Ghana. Contrib. Miner. Petrol. 129, 143–154.

Stachel, T., Viljoen, K.S., Brey, G., Harris, J.W., 1998. Metasomatic processes in lherzolitic and harzburgitic domains of diamondiferous lithospheric mantle: REE in garnets from xenoliths and inclusions in diamonds. Earth Planet. Sci. Lett. 159, 1–12.

Suhr, G., Seck, H.A., Shimizu, N., Gunther, D., Jenner, G., 1998. Infiltration of refractory melts into the lowermost oceanic crust: evidence from dunite- and gabbro-hosted clinopyroxenes in the Bay of Islands ophiolite. Contrib. Miner. Petrol. 131, 136–154.

Su, B., Chen, Y., 2018. Making cratonic lithospheric mantle. JGR: Solid Earth 123, 9. https://doi.org/10.1029/2018JB016179.

Tanaka, T., Togashi, S., Kamioka, H., Amakawa, H., Kagami, H., Hamamoto, T., Yuhara, M., Orihashi, Y., Yoneda, S., Shimizu, H., Kunimaru, T., Takahashi, K., Yanagi, T., Nakano, T., Fujimaki, H., Shinjo, R., Asahara, Y., Tanimizu, M., Dragusanu, C., 2000. JNdi-1: a neodymium isotopic reference in consistency with LaJolla neodymium. Chem. Geol. 168, 279–281.

Thomas, R.J., von Veh, M.W., McCourt, S., 1993. The tectonic evolution of southern Africa: an overview. J. Afr. Earth Sc. 16, 5–24.

Ulmer, P., Sweeney, R.J., 2002. Generation and differentiation of group II kimberlites: constraints from a high pressure experimental study to 10 GPa. Geochim.

Cosmochim. Acta 12, 2139–2153.

Vervoort, J.D., Patchett, P.J., Blichert-Toft, J., Albarède, F., 1999. Relationships between Lu-Hf and Sm-Nd isotopic systems in the global sedimentary system. Earth Planet. Sci. Lett. 168, 79–99.

Wainwright, A.N., Luguet, A., Fonseca, R.O.C., Pearson, D.G., 2015. Investigating metasomatic effects on the [187]Os isotopic signature: a case study on micrometric base metal sulfides in metasomatised peridotite from the Letlhakane kimberlite (Botswana). Lithos 232, 35–48.

Walker, R.J., Carlson, R.W., Shirey, S.B., Boyd, F.R., 1989. Os, Sr, Nd, and Pb isotope systematics of southern African peridotite xenoliths – implications for the chemical evolution of subcontinental mantle. Geochim. Cosmochim. Acta 53, 1583–1595.

Walter, M.J., 1998. Melting of garnet peridotite and the origin of komatiite and depleted lithosphere. J. Petrol. 39 (1), 29–60.

Wallace, M.E., Green, D.H., 1988. An experimental determination of primary carbonatite magma composition. Nature 335, 343–346.

Wittig, N., Baker, J.A., Downes, H., 2007. U-Th–Pb and Lu–Hf isotopic constraints on the evolution of sub-continental lithospheric mantle, French Massif Central. Geochim. Cosmochim. Acta 71, 1290–1311.

Wittig, N., Pearson, D.G., Duggen, S., Baker, J.A., Hoernle, K., 2010. Tracing the metasomatic and magmatic evolution of continental mantle roots with Sr, Nd, Hf and and Pb isotopes: a case study of Middle Atlas (Morocco) peridotite xenoliths. Geochim. Cosmochim. Acta 74, 1417–1435.

Wang, H.L., van Hunen, J., Pearson, D.G., 2018. Making Archean cratonic roots by lateral compression: a two-stage thickening and stabilization model. Tectonophysics 746, 562–571.

Woodland, A.B., Bulatov, V.K., Brey, G.P., Girnis, A., Höfer, H.E., Gerdes, A., 2018. Subduction factory in an ampoule: experiments on sediment–peridotite interaction under temperature gradient conditions. Geochim. Cosmochim. Acta 223, 319–349.

Woodland, A.B., Girnis, A.V., Bulatov, V.K., Brey, G.P., Höfer, H.E., 2019. Experimental study of sulfur solubility in silicate–carbonate melts at 5–10.5 GPa. Chem. Geol. 505, 12–22.

Yaxley, G.M., Crawford, A.J., Green, D.H., 1991. Evidence for carbonatite metasomatism in spinel peridotite xenoliths from western Victoria, Australia. Earth Planet. Sci. Lett. 107, 305–317.

Yaxley, G.M., Green, D.H., 1994. Experimental demonstration of refractory carbonate-bearing eclogite and siliceous melt in the subduction regime. Earth Planet. Sci. Lett. 128, 313–325.

Yund, R.A., Kullerud, G., 1966. Thermal stability of assemblages in the Cu-Fe-S system. J. Petrol. 7 (3), 454–488.